Chaotic mixing in a bounded three-dimensional flow

By G. O. FOUNTAIN[1], D. V. KHAKHAR[2], I. MEZIĆ[3]
AND J. M. OTTINO[1]†

[1]Department of Chemical Engineering, Northwestern University, Evanston, IL 60208, USA

[2]Department of Chemical Engineering, Indian Institute of Technology – Bombay, Powai, Mumbai, 400076, India

[3]Division of Engineering and Applied Science, Harvard University, Cambridge, MA 02138, USA

Even though the first theoretical example of chaotic advection was a three-dimensional flow (Hénon 1966), the number of theoretical studies addressing chaos and mixing in three-dimensional flows is small. One problem is that an experimentally tractable three-dimensional system that allows detailed experimental and computational investigation had not been available. A prototypical, bounded, three-dimensional, moderate-Reynolds-number flow is presented; this system lends itself to detailed experimental observation and allows high-precision computational inspection of geometrical and dynamical effects. The flow structure, captured by means of cuts with a laser sheet (experimental Poincaré section), is visualized via continuously injected fluorescent dye streams, and reveals detailed chaotic structures and chains of high-period islands. Numerical experiments are performed and compared with particle image velocimetry (PIV) and flow visualization results. Predictions of existing theories for chaotic advection in three-dimensional volume-preserving flows are tested. The ratio of two frequencies of particle motion – the frequency of motion around the vertical axis and the frequency of recirculation in the plane containing the axis – is identified as the crucial parameter. Using this parameter, the number of islands in the chain can be predicted. The same parameter – using as a base-case the integrable motion – allows the identification of operating conditions where small perturbations lead to nearly complete mixing.

1. Introduction

Osborne Reynolds, in a lecture delivered at the Royal Institution more than a century ago, in 1893, captured the essence of mixing (see Reynolds 1894; the lecture appears also in Reynolds's Complete Works, Reynolds 1901). In it he said: '… attenuation [thinning of fluid layers] is only the first step in the process of mixing – all involve the second process, that of folding, piling, or wrapping, by which the attenuated layers are brought together'. Someone reading this sentence with the hindsight of chaos theory cannot miss the transparent connection of Reynolds's 'attenuation' and folding to modern-day horseshoes, chaos, fluid mixing and everything that follows. But this little paper by Reynolds was not destined to be among Reynolds's masterpieces; at least two or three other papers dwarf it for acclaim. Many fluid mechanicians, though probably

† To whom correspondence should be directed: ottino@chem-eng.northwestern.edu.
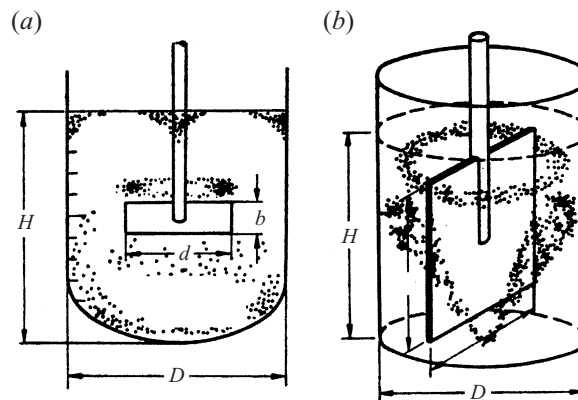
(a)   (b)

FIGURE 1. Drawings from Nagata's (1957, 1975) work depicting 'doughnut-like' structures or tori present within mixing tanks. Some lettering present in the originals has been removed.

not many mathematicians, may have read it. In any case, the stretching-folding/chaos connection was missed (for a brief historical account, see Ottino *et al.* 1992).

A somewhat similar story is Shinji Nagata's work in Japan. Nagata was one of the pioneers of mixing though, in this case, approaching the topic from a decidedly engineering viewpoint. In a ground-breaking book he classified all the knowledge of mixing in stirred tanks going back to work he had carried out since the mid 1950s (Nagata 1975). Figure 1, a sketch from one his early papers (Nagata, Yanagimoto & Yokohama 1957) and reproduced in his book, has undoubtedly been seen by most researchers in mixing. In the book the picture appears accompanied by the comment: '... a ring like a doughnut exists, and it is not mixed with other parts of the liquid for a long time ...'. To someone trained in dynamical systems and chaos the connection is hard to miss; Nagata's doughnut regions are non-chaotic or regular domains. Clearly, few people trained in dynamical systems appear to have come across Nagata's sketch. Had they encountered it, experimental studies of chaos in three-dimensional flows would have started sometime in the 1970s.

In recent years, significant strides have been made in the understanding of mixing. Most of the early momentum was due to studies of two-dimensional flows. Advances were largely spurred by developments in chaos theory (Wiggins 1991). Studies using idealized flows proved useful in visualizing structures (Ottino *et al.* 1988) and were instrumental in spurring applications in a wide range of fields ranging from chemical and polymer processing (Ottino 1994; Danescu & Zumbrunnen 1998; Tjahjadi & Foster 1995) to geophysics (Kellogg & Stewart 1991) and oceanography (Brown & Smith 1991; Joseph & Swathi 1999).

Most mixing flows of practical importance are three-dimensional. The number of experimental studies addressing full three-dimensional flows is, however, small. Remarkably, the very first simulation of chaotic advection was three-dimensional (albeit spatially periodic) (Hénon 1966). Michel Hénon's short two-page paper considered a Beltrami flow – a flow where the vorticity and velocity are co-linear (Aris 1962). Hénon's only figure, sketchy by today's standards, clearly shows chaotic trajectories as well as regular regions. The work, however, was ahead of its time. Except for a brief study by Philip Holmes in 1984 (Holmes 1984) no references appear until the late 1980s.

Hénon's study can be traced to a note published by Vladimir Arnold in 1965 on

the integrability of three-dimensional Euler flows (Arnold 1966). Arnold asserted that three-dimensional Euler flows are integrable except possibly in the case when vorticity and velocity are parallel (the case of so-called Beltrami flows). Based on this result, Arnold suggested a class of special solutions of Euler's equation, now the so-called ABC flows (Dombre *et al.* 1986) – after Arnold, Beltrami and Childress – as possible non-integrable flows. This was the flow considered by Hénon.

But most of the work to date has concentrated on two-dimensional flows. The interest in chaotic advection took off when a numerical study by Aref advanced the concept of chaotic advection in terms of the 'blinking vortex flow' (Aref 1984). This was quickly followed by an analytical study (Khakhar, Rising & Ottino 1986) and experimental studies (Chaiken *et al.* 1986; Chien, Rising & Ottino 1986; Ottino *et al.* 1988; Swanson & Ottino 1990). These early studies were two-dimensional and used the fact that motion of fluid particles in two-dimensional, time-dependent area-preserving fluid flows is governed by a one-and-a-half degree-of-freedom Hamiltonian system. One exception is a study by Khakhar, Franjione & Ottino (1987) which focused on mixing in an unbounded steady three-dimensional flow in a continuous flow system.

A systematic study of issues arising in three-dimensional flows started with the paper of Feingold, Kadanoff & Piro (1988). Starting in the 1990s a number of numerical studies (Bajer & Moffatt 1990; Stone, Nadim & Strogatz 1991; Holm & Kimura 1991; Ashwin & King 1995, 1997; Rudman 1998; Bryden & Brenner 1999; Kroujiline & Stone 1999) helped in understanding some of the phenomena that occur in three-dimensional flows. Feingold *et al.* (1988) emphasized that the two prototypical types of situations that occur in three-dimensional volume-preserving maps can be understood on the basis of perturbative studies of the so-called *action-angle-angle* and *action-action-angle* maps (see below). Mezić & Wiggins (1994) show how these two types of maps arise from the symmetries of the flow and identify typical three-dimensional flow situations in which these maps occur – a vortex ring flow with swirl (action-angle-angle) and without swirl (action-action-angle). That idea was taken further in Haller & Mezić (1998) and Yannacopoulos *et al.* (1998) where the notions of *geometrical symmetries* (those arising from the geometry of the apparatus) and *dynamical symmetries* (those that arise due to the equations of motion of the fluid) are introduced, linking the motion of particles to the physics of the flow. Our analysis in this paper hinges mostly on the concept of action-angle-angle flows, symmetries, and the ideas of flow skeleton introduced in MacKay (1994).

Experimental counterparts are few and many focus on systems that are often too complex to permit theoretical treatment. Peerhossaini, Castelain & Leguer (1993) and Acharya, Sen & Chang (1992) studied chaotic mixing in three-dimensional flows in pipes; the focus of these two papers was transport enhancement. The main study on visualization in three-dimensional flows is the work by Kusch & Ottino (1992) focusing on a chaotic advection in two types of three-dimensional continuous flows. One of these systems, the partitioned pipe mixer (Khakhar *et al.* 1987) consists of a pipe and series of flat partitions at right angles to each other spanning the diameter of the pipe. Experimental studies clearly show regular and chaotic regions.

A few works have concentrated on realistic mixing tanks. Muzzio and co-workers carried out experimental studies (Lamberto *et al.* 1996; Lamberto, Alvarez & Muzzio 1999) that show toroidal structures such as those of Nagata in figure 1. Numerical simulations in different types of tanks (Harvey & Rogers 1996; de la Villéon *et al.* 1998) show the co-existence of chaos and order and regular islands (cuts through regular tori) though it is not clear if they were aware of Nagata's prediction. In any case, the amount of theoretical treatment in these systems is limited. Clearer

connections with theory can be found in the works dealing with Taylor–Couette flows (Ashwin & King 1995, 1997; Rudman 1998).

Objectives and scope of the paper

The objective of this paper is to present an experimental system that serves as a prototype for studies in three-dimensional bounded flows. The aim was to find a configuration that is simple enough to be scrutinized in terms of high-precision numerics, but at the same time realistic in the sense that it can be built and detailed experimental inspection is possible. Moreover, from a theoretical viewpoint, it was desired to have a small parameter of geometrical origin (rather than a Reynolds number alone) to allow the separation of geometrical and dynamical effects.

The system considered here is an idealization of a mixing tank and it is inspired by the 'flow within a drop' system of Bayer & Moffatt (1990) and Stone *et al.* (1991). This is an idealized flow within a spherical drop of a viscous fluid induced by a combination of a three-dimensional hyperbolic flow and a twisting flow ω mimicking a vortical flow. The angle between the principal axis of compression or extension and the axis of rotation ω is denoted α. If $\alpha = 0°$, the flow is regular; if $\alpha > 0°$ then the flow is chaotic, with Poincaré sections (mappings formed by the repeated intersections of fluid trajectories with a specified surface) showing a classical picture of KAM-tori and chaotic tangles.

The apparatus (figure 2) considered here consists of a cylindrical tank (diameter T) with a flat disk impeller (diameter D); both the impeller, I, and the tank, T, can be rotated at angular speeds N_I and N_T, respectively, and the angle of the impeller with respect to the vertical, α, can be changed. Two Reynolds numbers can be thus defined: $Re_I = N_I D^2 \rho/\mu$, $Re_T = N_T T^2 \rho/\mu$, where ρ and μ are the density and viscosity of the fluid, respectively. As we shall see, both can be varied experimentally in the range $0 < Re_I < 200$, and $0 < Re_T < 10$ (with glycerine).

To achieve chaotic behaviour, the impeller angle is adjustable. A non-trivial change is that produced by the motion of the tank wall. Primary attention will be paid to the region below the impeller.

The paper is structured as follows: §2 presents the experimental set-up and techniques. Section 3 provides a description of the perturbative theory of mixing for three-dimensional, steady flows based on Feingold *et al.* (1988), Mezić (1994), Mezić & Wiggins (1994), Haller & Mezić (1998) as well as discussion on the possible mixing structure corresponding to high-Reynolds-number flows. Section 4 covers the details of the numerical simulations. Section 5 discusses the results of the experimental and numerical study and shows how they tie in with the theoretical framework. Finally, conclusions are presented in §6.

2. Experimental details

2.1. *Apparatus*

The basic design of the apparatus is that of a rim-suspended cylindrical tank fabricated from a transparent material. Through the use of motors, the tank can be rotated along its vertical axis in either direction. Supported on the same frame as the tank, a shaft terminated by a disk impeller is positioned in the tank in such a way that the angle of the impeller shaft can be varied continuously from vertical ($\alpha = 0°$) to a maximum angle of 20°. See figure 2 for an overview.

The design begins with the tank. Two types are used, primarily based on convenience and cost. For detailed measurements, where optical effects are critical (see PIV
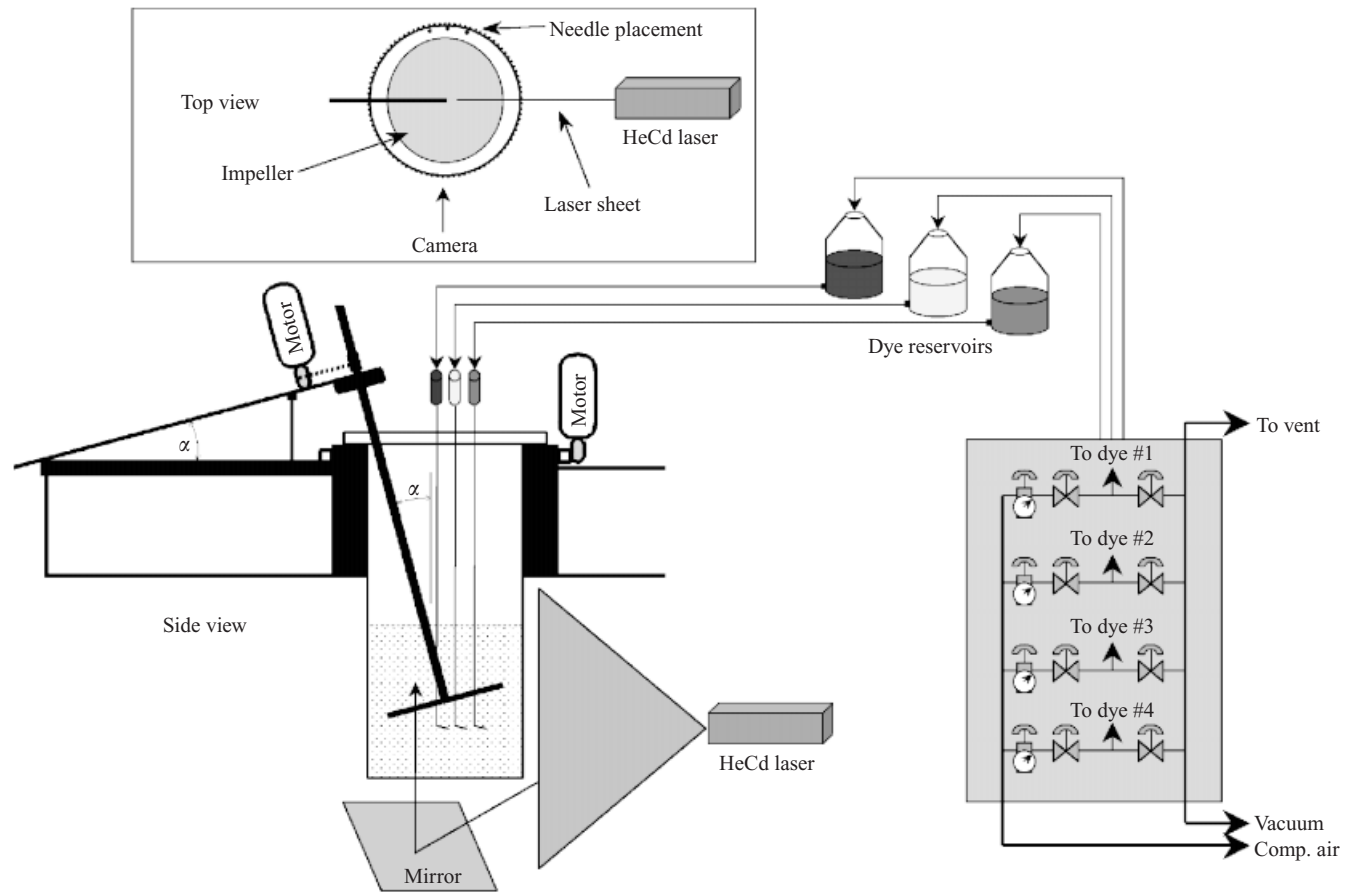
FIGURE 2. Schematic of tank assembly. Dye injection is controlled by the pressure manifold. Each individual dye reservoir can be independently regulated with both compressed air and vacuum.

discussion, §2.8), an acrylic tank is used. The tank measures 13 cm (5.1 in.) in inside diameter and 30 cm (11.8 in.) in internal height. The tank walls are formed from cast acrylic tubing (Townsend Plastics) measuring 14 cm (5.5 in.) in external diameter and with 0.5 cm (0.125 in.) wall thickness. The bottom is closed by way of a 1.3 cm (0.5 in.) piece of acrylic sheet stock joined with a rabbetted edge for additional gluing surface. The top of the tank has a machined acrylic flange 2.5 cm (1.0 in.) wide made from 1.3 cm (0.5 in.) sheet stock. The flange is also cut to provide additional gluing surface between the flange and tank cylinder, as it must support the weight of the entire assembly when filled with fluid. Four alignment holes are set into the bottom face of the flange to provide positive positioning as well as to prevent any possible tank slippage during rotation. The individual pieces are glued using acrylic solvents. Additional tanks manufactured from Pyrex® glass are used when optical distortion effects were less critical. These also have an inside diameter of 13 cm (5.1 in.) and are either 30 cm (11.8 in.) or 20 cm (7.9 in.) in internal height.

External to the tank is a rectangular box also constructed from acrylic panels supported by an aluminium frame and clamped to the tank support assembly. Extra care was taken during the manufacture of the external box to ensure that all surfaces were perpendicular. This is then filled with either pure glycerine (for dye photos) or index-matched glycerine (see §2.4) for PIV studies. The purpose of the external fluid-filled vessel is to minimize the optical distortion due to the curved glycerine–wall–air interface.

An external framework supports the entire assembly. Two items of importance are the rotatable mount sleeve for the tank and the impeller mount platform. The tank is supported through a mounting sleeve that has gear teeth along its circumference. The sleeve is then rotated by means of a motor. Speed and direction are controlled through the use of a Bodine® motor control. The impeller assembly is supported on a raised platform that is parallel to the top surface of the tank.

Finally, the impeller assembly consists of an alignment plate to which the motor is mounted, two bearing mounts, and the impeller shaft terminated by the impeller. The alignment plate has a machined channel along the long axis that matches with a raised spline on the support platform to provide positive alignment. The angle is controlled using a pair of support bolts opposite the pivot point on the support platform. The impeller shaft is mounted on the plate through two needle bearings (7.5 cm apart) to minimize any wobble in the shaft. The drive gear is mounted between the bearings and is connected to the motor by means of a timing belt. The shaft is fabricated using a length of 1.3 cm (0.5 in.) diameter, centreless ground stainless steel rod 50 cm (20 in.) long. The impeller is a lathe-turned disk of 0.48 cm (0.19 in.) thick acrylic. The impeller diameter is 10.2 cm (4.0 in.). The impeller is driven with a Compumotor® S-series stepper motor and is controlled using a Compumotor® AT-4800 computer interface board. The shaft length is adjustable (along with the alignment plate angle) to position the impeller at the proper location. Once the angle and impeller length have been set, the alignment plate is clamped to the support platform. Viewing down from the top of the tank allows designation of the impeller and tank rotations. Clockwise rotation is designated + and counter-clockwise rotation −. An example of the computed velocity field generated in the device when operated in the counter-rotational case is shown in figure 3.

2.2. *Photography*

Photographs were taken to record the experimental results. Standard 35 mm SLR cameras were used; a Nikon N2000 with Nikkor 105 mm (1 : 2.5) lens and a Nikon
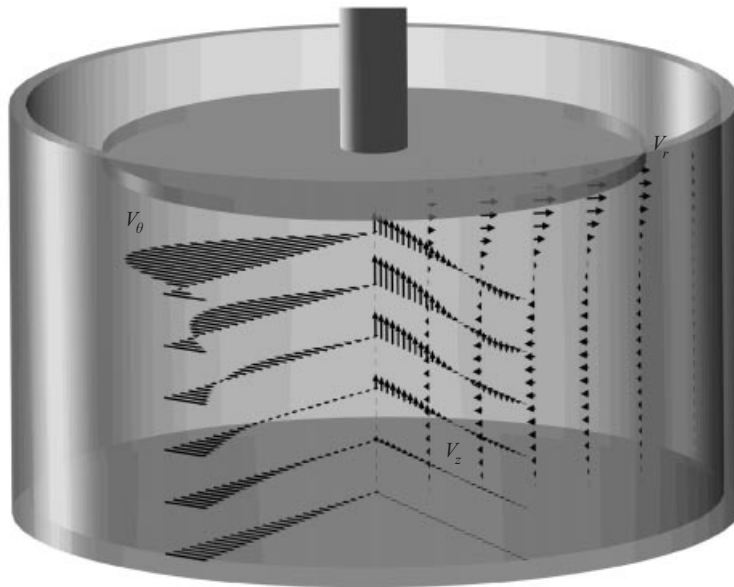
FIGURE 3. Velocity profile for fluid in lower half of tank ($\alpha = 0°$, $N_I = 30$ RPM, $N_T = -3$ RPM). Vectors indicate $v_\theta(r, \theta = \text{const}, z)$, $v_z(r, \theta = \text{const}, z)$, and $v_r(r, \theta = \text{const}, z)$. Note: v_θ is shown at 50% of true magnitude for clarity.

FE2 with Nikkor 105 mm (1 : 4) lens. Due to the unusual lighting conditions, exposures were bracketed for most runs, especially at the early stages of each experiment. Typical exposure times using Kodak Elite Chrome (and Elite II) 400 slide film were 0.5–4 s. Higher speed film (Ektachrome 1600) was also used, but without noticeable improvement. The primary trade-off is slight smearing with longer exposures vs. larger grains on the high-speed film.

Photographs were taken from two primary perspectives. These perspectives then dictate positions in the following discussions regarding placement of equipment. The primary camera (35 mm) was positioned in 'front' of the setup looking directly at the sidewall of the tank and such that the external chamber (and laser sheet) is perpendicular to the camera (to minimize optical effects). A second camera was used to capture shots from an angle, typically from above and to the left of the primary camera. It was also used for close-up images. A yellow filter was used on the primary camera to eliminate any blue scatter from the laser. Additional lighting was provided on some photos using a standard hand-held UV test light (BayCo SMART™ 9W fluorescent, Dallas, TX).

2.3. *Lasers*

A sheet of laser light cast across the flow system is used to form an experimental Poincaré section. For the dye experiments, a Liconix 4240NB helium–cadmium constant-wave laser, capable of 442 nm (blue) and 325 nm (UV) operation, was used with the 442 nm optics installed. The power rating at this wavelength is a nominal 40 mW and was verified after tuning at 36 mW using an Ophir laser power monitor. The light sheet was created using a 2 mm cylindrical rod lens mounted on the laser head and aligned such that the sheet fell vertically on the centreline of the impeller shaft. The laser is positioned to the right of the tank and the beam crosses from right to left. As the beam diverges with the cylindrical lens, there is more light intensity

available in the right-half portions of the experimental photographs than the left. To overcome some of the deficiency in intensity, a mirror was used to reflect a portion of the sheet from below the system upward. An additional benefit of this reflection is that it is possible to illuminate the otherwise shadowed area in the quadrant above the impeller and to the left of the impeller shaft. Small alignment errors in using the secondary mirror have negligible effect on the final photographs.

For the PIV studies, a dual-YAG (yttrium–aluminium–garnet, 532 nm) laser system from TSI Inc. was used. Each laser has a pulse intensity of 25 mJ with a pulse width of 5–7 ns. Two lenses are used on the laser head, one focal (1 m), the other a cylindrical sheet lens. The system was imaged in two sections (left and right), mitigating the need for balancing the intensity between the two sides. Thus, the mirror was not required for the PIV studies. This also eliminates any possible alignment errors that would affect the sheet thickness and introduce possible errors into the velocity calculations.

2.4. *Fluids*

The primary fluid used in all of the experiments was USP grade (99.7%) glycerine. The true viscosity was measured with a Bohlin rheometer for the experimental temperatures (typically 21 °C–22 °C). Additionally, since glycerine is hygroscopic, periodic checks for water contamination of the glycerine supply were made using a Nautilus model 4540 viscometer (see the Appendix). For the experimental PIV measurements, powdered sodium iodide (NaI) was added at 17.7 wt% to alter the index of refraction of the glycerine to match that of the acrylic walls (for the wavelength of the YAG laser). Batches of approximately 20 l were made at a time to ensure sufficient surplus to complete each series of experimental runs. The initial refractive index calibration was made using a Milton Roy model ABBE-3L refractometer (see figure 23, Appendix) and final corrections were made by checking for beam deflection with the YAG laser before the experiments. This index-corrected glycerine is then used both in the tank and in the external rectangular containment vessel. Unless this step is taken, the optical distortions due to the curved tank wall significantly impact the accuracy of the velocity field measurements.

2.5. *Dyes and particles*

Visualization is achieved with laser-grade fluorescent dyes dissolved in glycerine. Specific dyes used in these runs were fluorescein (Sigma F-6377), fluorexon (Aldrich 11,985-7), rhodamine 6G (Baker U-874), sulforhodamine B (Kodak 14321), and LDS 698 (Exciton 06980, aka pyridine 1). For a majority of the runs only fluorexon (green emission), rhodamine 6G (yellow emission), and LDS 698 (red emission) were used. Dyes were selected both for their absorption characteristics as well as for the colour of their emissions. Another consideration is to minimize coupling between dyes where the emission of one (in plane) dye can cause another (out of plane) to absorb and re-emit thus obscuring the view. The primary difficulties in the preparation of the dyes were clumping of the powders in the glycerine, strong adhesion to the beaker walls, and slow dissolution rates. To minimize clumping, the dyes were measured out into a small beaker pre-filled with approximately 10 ml of glycerine to prevent the dye from sticking to the bottom and sides. Then the mixture was stirred to disperse the powder and poured off into a larger, pre-weighed 500 ml container. Additional glycerine was added to the beaker, the sides scraped and this too was added to the large container. This was repeated until the beaker was clear. Finally, the 500 ml container was topped off with glycerine and capped. It was then inverted several times periodically over the course of several days until all of the dye had dissolved.

Typical concentrations of dye used in these experiments ranged from 1.3×10^{-4} wt% to 2.4×10^{-4} wt%. Correspondingly, the active dye concentrations ranged from 0.34 mM to 0.49 mM. Due to the extremely low concentrations, density and viscosity variations were considered to be negligible.

For the PIV measurements, reflective particles were seeded into the flow. The particles used in these experiments were Dow Saran glass beads, 16 μm in diameter with a density of 1.63 g cm^{-3}. Approximately 0.5 cm^3 of particles were used for the tank (0.3 cm^3 l^{-1} of fluid). The viscosity change due to the particles is negligible ($\sim 0.075\%$).

2.6. *Injection system for dyes*

To inject the dyes into the system, long thin-walled needles supplied from pressurized reservoirs were used. A pressure manifold was constructed (see figure 2) consisting of four channels, each with a pressure regulator (McMaster-Carr) and two valves. Tygon tubing was used for all connections and secured with hose clamps. The manifold allows each reservoir to be at, above, or below atmospheric pressure. The manifold is supplied by house compressed air (through a bed of Dri-Rite desiccant) and by an aspirator (with trap) for vacuum.

Each outlet tube from the manifold connects to the top of a dye reservoir. Dye is fed from the reservoir through a tube to a syringe (10 cm^3 plastic medical syringes with the plunger removed). The needles were built up from 18 and 20 gauge (1.3 and 0.9 mm OD respectively) thin-wall stainless steel micro-tubing (McMaster-Carr). Each needle was 30.5 cm (12 in.) long and epoxied into a Luer hub for attachment to the prepared syringes. At the opposite end of each needle there was a 90° bend ($\varnothing \sim 1$ cm) approximately 3 cm from the end to allow positioning into the flow from along the outer wall. The needles are held in position within the tank using clamps supported along the rear of the tank behind the plane of the laser when viewed from the camera position.

2.7. *Experimental procedure for dye photographs*

In preparation for the experimental dye photographs, tanks were filled with glycerine to a height of 13 cm and allowed to sit (at a minimum overnight). This allows time for the small bubbles that are generated during pumping to rise to the surface and also to ensure that the temperature has equilibrated with the rest of the apparatus (primarily the external glycerine-filled chamber). The tanks are sealed with a double layer of Parafilm to prevent water from being absorbed into the glycerine. For the external chamber, any water-diluted layer on the surface is removed and additional fresh glycerine is added. The glycerine in the external chamber is then lightly stirred to remove small optical differences due to slight differences in water content between the old and new glycerine. Care is taken to not introduce any bubbles. At least one hour before the experiments, the laser is turned on to allow it to come to full intensity.

Once the external frame has been checked for level (and adjusted if needed using leg levellers), the filled tank is positioned through the sleeve and into the external chamber. The tank wall motor is turned on both for checking the centre alignment of the tank (by observing any precession) as well as providing additional mixing to the external chamber. For those runs where the tank wall is to be rotated, the motor is run a minimum of 20 minutes to allow it to warm up.

The impeller is lowered into the tank and fastened to the mount platform. The angle is controlled by adjusting two threaded bolts that support the leading edge of the alignment plate. The rear edge is clamped to the opposite end of the mount platform
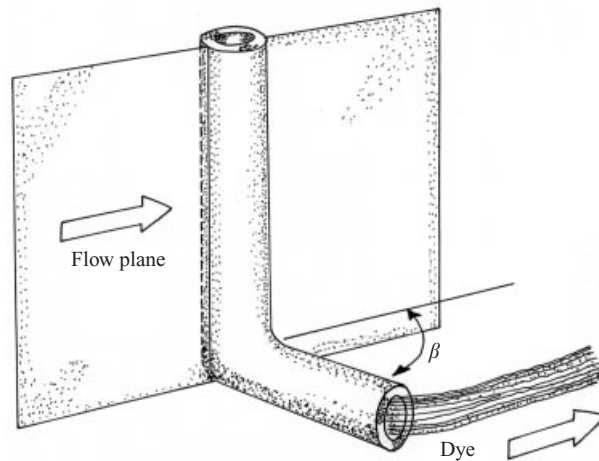
FIGURE 4. Injection needle placement relative to local flow. The downstream position prevents spreading of the dye as it leaves the tip.

once the impeller is centred. The impeller is centred horizontally and vertically by using an alignment grid positioned on the external chamber. Alignment 'front–back' is provided directly by the spline in the mount platform. For all the experiments presented here, the impeller is positioned in the centre of the tank, 6.5 cm from the bottom and 6.5 cm from the walls. Once in position, the impeller motor is started and allowed to warm up for a few minutes.

Just before the start of each experimental run, the dye needles are prepared. The end of each needle is placed into a fresh beaker of glycerine and a slight vacuum is applied to the reservoirs. This forces a small amount of clear glycerine to be pulled up into the needle and prevents any dye from being released before it is in position. Without this step, each needle would leave a small 'tail' behind it while being inserted, or worse, during the run. Care must be taken not to pull too much clear glycerine into the needle. Once a sufficient amount of clear glycerine is drawn into each needle, the vacuum is relieved before the needle is removed from the beaker. If this is not done, air will be drawn into the needle and will result in bubbles in the flow during injection. Each needle is then placed in the tank and positioned along the tank wall behind the plane of the laser. The tips, which are bent to lie horizontally, are positioned such that they point in the direction of the local flow, thus lying along the wall itself (and thus minimizing their effect on the flow). The needles are also positioned such that they are either along or above the centreline of anticipated core tori. This is usually done qualitatively although some were positioned using reference marks determined by numerical simulations or previous experiments. Small errors here are not critical. Vacuum may again be applied briefly depending upon the length of time between initial preparation and start of the actual run to avoid leakage due to gravity or siphoning.

Each colour is then injected in the same manner. The impeller (and tank wall, when used) is set to the proper rotational rate. The pressure manifold is set initially to 20 p.s.i.g. on each regulator (but each needle is still isolated due to the valves). The first needle is rotated into position (for the centremost dye stream) and pressure applied to its reservoir. Again, the tip is oriented in a downstream manner as shown on figure 4. Without doing this, the dye has a tendency to 'blossom' around the tip

of the needle making the dye stream significantly wider. This reduces detail observed in the photographs. The experimental clock is started upon initial release of the dye stream. Dye is then allowed to flow until the structure it is following is sufficiently well defined. For the inner tori, this is typically fairly quick (less than 2 minutes). The outermost structures may require up to 10 minutes. The rate of dye injection is controlled by adjusting the supply air pressure. At the maximum driving pressure used of 25 p.s.i.g., the dye flow rate is 0.6 ml per minute for the largest bore needles used. Photographs are taken periodically during the injection sequence by the primary camera. Photos from the secondary camera are taken as needed.

Once sufficient dye has been injected from a given needle, the valve supplying pressure to the reservoir is turned off and vacuum is applied for 5–10 s. This again prevents a dye tail from following the needle as it is slowly rotated back along the wall. Now, using the first dye structure as a guide, the next needle is positioned and the procedure repeated. An example of the intermediate photo from an angled perspective is shown in figure 5. The torus formed by the dye is clearly visible (figure 5a). A cross-sectional cut (figure 5b) shows the torus to have a jagged surface; this is due to the disturbance caused by the needle and is discussed in more detail below (§2.9). As the structure is built up, needles are carefully removed once they are no longer needed. This is done to minimize their effect on the flow as the structures approach the outer wall. Also, the injection point is higher and higher, in general following a line approximately 45° up and to the wall from the centremost torus. Once the final injection has been made and the needle removed, the system is allowed to continue running for at least one hour (total time for the injection sequence is typically on the order of 40 minutes) and often three to four hours. With such a long steady relaxation time, we can be certain that the effect of the needles on the final structures is eliminated. Final photographs are taken to record the relaxed state of the system.

2.8. *Experimental procedure for PIV*

Experimentally, the requirements for the PIV measurements are much less complicated than those for the dye advection, but require strict attention to optical effects. The set-up begins in a similar fashion to the dye studies. The primary difference is the fluid. As detailed in §2.4, the refractive index must be matched between the vessel walls and the fluid. To achieve this, NaI was added. Also, since glycerine is strongly hygroscopic, the prepared fluid must be kept sealed from the atmosphere as much as possible. It is stored in an airtight container. Before and after runs, the filled tank is kept covered with a double layer of Parafilm. For runs that do not require moving the outer tank wall, the top of the tank is kept covered except for the small portion required for the impeller shaft to pass. Plastic wrap was placed over the square outer chamber when exposed. The fluid in both is periodically replaced.

The laser assembly is mounted on an optical lift table that permits accurate *x-z* positioning. To align the experimental assembly, the laser is used without the sheet lens and the beam is passed through reference marks on the acrylic walls. Once everything is squarely aligned the sheet lens is remounted and the sheet is aligned vertically with the impeller shaft. The distance between the laser head and the centre of the tank is approximately 1 m to match the focal length of the lens and minimize the sheet thickness during measurement.

A software/hardware bundle from TSI handles data collection. Briefly, it consists of a PC with a frame grabber and a synchronizer connected to an 8-bit greyscale CCD camera. The camera has a resolution of 640×480 pixels and is capable of 30
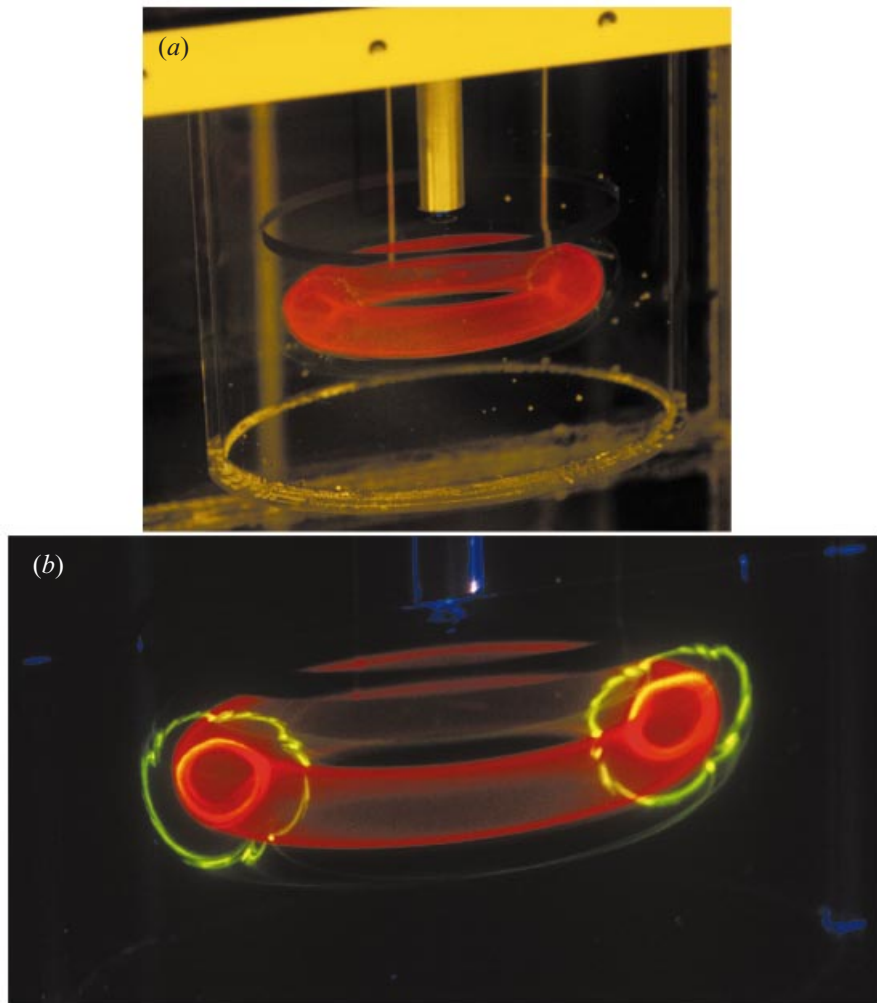
FIGURE 5. Perspective view of tori ($\alpha = 0°$, $N_I = 30$ RPM, $N_T = 0$ RPM, $Re_I = 6.5$). (*a*) Photographed with the room lights on. One can see the faint outline of the laser sheet along the surfaces of the red tori. The green dye is not excited to the same degree and is almost invisible. (*b*) The same view, but with the room lights extinguished. A weak UV lamp has been placed above the system to add mild supplemental illumination. Here the detail provided by the laser cut is quite dramatic.

frames per second. Frame straddling is used to achieve frame pairs with less than 33 ms separation. Data are acquired and stored to RAM during each run and then written to disk at the end. Post processing is then performed on the image data to obtain the velocity information. The software uses two-frame cross-correlation to determine the in-plane velocity components.

For each experimental condition, the lower half of the tank was imaged in two sections (left and right). This gave greater spatial resolution and reduced the amount of intensity variation across a single frame. Since the flow was steady, it was possible to collect multiple frames and average to improve the reliability of the data. One concern is that since PIV collects the in-plane velocity components, in this case v_r and v_z, and the flow is primarily in the θ-direction, there will be insufficient particle

residence time in the sheet, or there will be insufficient in-plane motion to obtain an accurate reading. To help overcome this, a spectrum of frame separation times (20 ms, 25 ms, 30 ms, and 40 ms) was used with 50 frame pairs taken at each time.

The raw data are processed by first using TSI's cross-correlation software to generate the velocity vectors for each frame pair. The frames were subdivided into overlapping 32×32 pixel domains giving a velocity grid of 40×30. A Whittaker search algorithm was used. To post-process the velocity vectors, the resulting 50 velocity fields were checked for consistency position by position. Any vectors that statistically deviated from the others (typically due to a high error in the cross-correlation) were eliminated from the ensemble and then an average was taken at each point. Consistency between different frame separation times was good and these data were then combined. This was needed due to the large variations in in-plane velocities present, for example near the impeller tip and near the tank bottom.

The results of the PIV studies were used in conjunction with the dye advection studies to validate the numerical simulations. A comparison between the PIV data and the numerical results is discussed in §4.1.

2.9. *Sources of error and consequences*

The major sources of error come from optical parallax and dye injection devices. While it is simple to see where optical effects can drastically affect the results of the PIV experiments, the dye advection studies are a bit more interesting when it comes to the consequences of errors. The obvious major source of error in the dye experiments is the presence of the needle itself in the flow. As it turns out, while the intermediate effects of the needles on the results can be severe, with sufficient precautions, the long-term observations can be shown to be robust and reliable.

One illustrative example can be seen in figure 6. Here an attempt was made to capture dye at the very centre of the period-1 (centremost) torus. The plan was simple: perform the experiment twice. At the end of the first experiment (figure 6a), a laser pointer was used to triangulate on features of interest (making marks on the external square vessel corresponding to the beam crossings). Then the experiment was repeated with fresh fluid and the reference points used to position the needle tip. In hindsight, the results should have been predictable. As can be seen in figure 6b, rather than the period-1 torus we knew to be present, the needle perturbation stimulated the formation of a period-4 torus. This can be seen in perspective in figure 6c. The experiment was continued and the structure allowed to relax after the needles were removed. The final result was the same as the first experiment (figure 6d).

Another error that can mask, or enhance, the small toroidal structures we are seeking occurs during needle movement. While the needle wake has an obvious effect, during repositioning care must be taken to avoid distorting the dye already laid down. Since the needles are supplied by tygon tubing, they have a tendency to twist. This, coupled with the significant length of the needles, can result in a jerky motion at the needle tip instead of a slow, smooth movement. Small errors during repositioning can result in wave-like perturbations being introduced whereas larger errors can cause destruction of all observable structures. The small waves tend to damp out and cause blurring of the toroidal surfaces. This type of error can be put to good intentional use though. In analysing the Poincaré sections, it is sometimes difficult to identify all of the islands present, as there are invariably gaps in the dye coverage (one cannot place the layers too closely together due to concerns of needle effects). The islands are usually observed by noting the regions where the dye does *not* penetrate and thus inferring the island structure. By causing
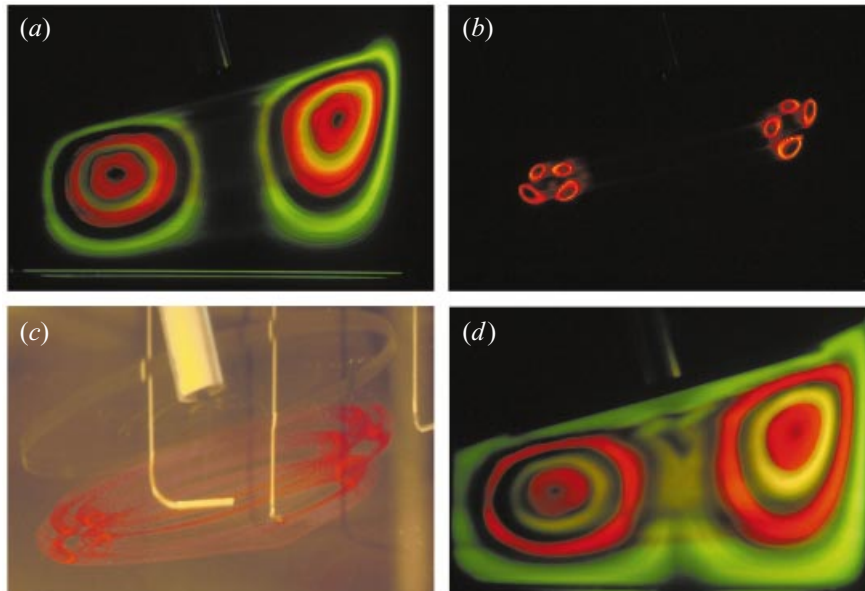
FIGURE 6. Needle effects. Needles placed into the system cause disturbances to the flow patterns. In this example, an experiment was repeated with the same conditions. (*a*) Final condition of a run ($\alpha = 15°$, $N_I = 30$ RPM, $N_T = 0$ RPM, $Re_I = 6.5$) over an hour after final needle removed. (*b*) Experiment restarted with fresh fluid using previous run to locate centremost tori. This results in a period-4 torus rather than a simple period-1. (*c*) Side view of the structure with room lights on. (*d*) Experiment continued to completion and needles removed. The same final state is reached and centre period-4 torus relaxes back to expected structure.
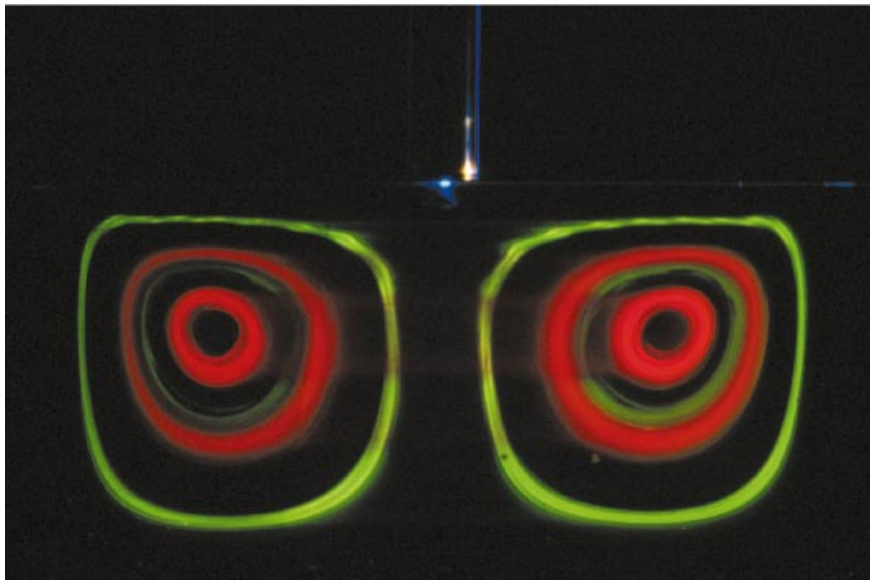

FIGURE 8. Unperturbed case ($\alpha = 0°$, $N_I = 30$ RPM, $N_T = 0$ RPM, $Re_I = 6.5$).

intentional smearing (and a little luck), the different concentrations of dye that remain in various regions will result in a significant coverage increase and good contrast enhancement. This is how the structures in figure 12 were photographed and identified.

3. Theoretical setting

The perturbative theory of mixing for three-dimensional, steady flows is based on Feingold *et al.* (1988), Mezić (1994), Mezić & Wiggins (1994), and Haller & Mezić (1998); a brief review of the main elements is presented here. Let us first recall the two-dimensional case. The kinematics of two-dimensional, area-preserving, time-dependent flows with simple time dependences (periodic, quasi-periodic) is now well understood and many examples have been studied (see, for example, Ottino 1989). These flows admit a simple characterization due to incompressibility: they are one-and-a-half degree-of-freedom Hamiltonian systems and can be written as

$$\dot{x} = -\frac{\partial \psi(x, y, t)}{\partial y}, \quad \dot{y} = \frac{\partial \psi(x, y, t)}{\partial x}. \tag{3.1}$$

where ψ, the stream function, corresponds formally to the Hamiltonian. When there is no dependence on time, the kinematic properties of the flow are simple: pathlines are equivalent to streamlines and fluid particles sample a very restricted portion of the physical space. Material lines stretch as t (Ottino 1990). The extent of mixing achieved without molecular diffusion is, in general, very small. Time dependence of (3.1) introduces a whole new set of phenomena: even without molecular diffusion, very good mixing properties can be achieved by pure stirring. If the two-dimensional flow studied is time-periodic, a Poincaré map can be constructed to obtain a two-dimensional area-preserving map (Wiggins 1990). Two-dimensional area-preserving maps have been studied in detail, a paradigm example being the standard map (Lichtenberg & Lieberman 1992). Geometrical features such as KAM-tori, cantori, and resonance zones have been extensively studied and a lobe dynamics theory of transport was developed by Rom-Kedar & Wiggins (1990, 1991), Rom-Kedar (1988, 1990), Rom-Kedar, Leonard & Wiggins (1990) and Wiggins (1991). All of these tools have been developed specifically to study the kinematics of mixing of two-dimensional area-preserving flows.

The main problem faced in the study of three-dimensional flows is the lack of a clear starting point; while equation (3.1) serves as the starting point for the analysis of two-dimensional flows there is no analogue for full three-dimensional flows. More specifically, steady volume-preserving three-dimensional flows cannot, in general, be cast in the Hamiltonian form, for which most results are available. To see this consider an arbitrary two-degree-of-freedom, autonomous Hamiltonian system given by

$$\dot{x} = -\frac{\partial \psi}{\partial y}, \quad \dot{y} = \frac{\partial \psi}{\partial x}, \quad \dot{z} = -\frac{\partial \psi}{\partial w}, \quad \dot{w} = \frac{\partial \psi}{\partial z}, \tag{3.2}$$

where (x, y, z, w) defines the four-dimensional phase space and the Hamiltonian $\psi(x, y, z, w)$ is time-independent. The Hamiltonian is hence a constant of the motion and only three of the four variables are independent. This implies that every two-degree-of-freedom autonomous Hamiltonian system defines a steady three-dimensional flow (e.g. (v_x, v_y, v_z)). The converse, however, is not true because the form given in equation (3.2) requires that

$$\frac{\partial v_x}{\partial x} + \frac{\partial v_y}{\partial y} = 0 \quad \text{and} \quad \frac{\partial v_z}{\partial z} + \frac{\partial v_w}{\partial w} = 0, \tag{3.3}$$

which is the condition that each pair of velocity components must conserve area. Some categories of steady three-dimensional flows can, however, be cast in a simple form that retains some of the structure of equation (3.2) by means of appropriate transformations as shown by Mezić (1994), Mezić & Wiggins (1994) and Haller &

Mezić (1998). These are flows that admit the volume-preserving symmetry. Well-known examples of this are: (i) continuous unbounded flows with a dominant axial component with an axial symmetry, and (ii) bounded flows with a strong azimuthal component with a rotational symmetry. In both these cases the velocity field becomes

$$\dot{x} = -\frac{\partial \psi(x, y)}{\partial y}, \quad \dot{y} = \frac{\partial \psi(x, y)}{\partial x}, \quad \dot{z} = F(x, y), \tag{3.4}$$

where F is a function arising from the transformation of coordinates, and forms the basis for analytical, perturbative studies of divergence-free viscous flows of the types given above. Category (i) flows include steady duct flows (Khakhar *et al.* 1987; Franjione & Ottino 1994); in particular, the experiments on three-dimensional chaotic advection performed by Kusch & Ottino (1992) accept interpretation in terms of perturbations of equation (3.4) (Mezić & Wiggins 1994). A specific situation in which this result applies is that of rotational symmetry (category (ii)), which is the case in our system when the angle $\alpha \equiv 0°$. Then ψ is just the streamfunction for the transverse velocity components of an axisymmetric, swirling flow. However, the relevance of the theory and the experiments presented here is much more general; for example, every Euler flow admits a symmetry such that it can be cast in the form (3.4) (Mezić 1994; Mezić & Wiggins 1994; Haller & Mezić 1998).

If the flow given in equation (3.2) is bounded and regular, it can be written, by means of coordinate transformations, in terms of action-angle variables (I, ϕ, J, θ) as (Arnold 1978)

$$\dot{I} = 0, \quad \dot{\phi} = \frac{\partial \psi}{\partial I}, \quad \dot{J} = 0, \quad \dot{\theta} = \frac{\partial \psi}{\partial J}, \tag{3.5}$$

with the Hamiltonian given by $\psi = \psi(I, J)$. Similarly, when a three-dimensional, steady flow has a volume-preserving symmetry, we can have two types of flows (Mezić & Wiggins 1994): *action-action-angle* flows $(\dot{I}, \dot{\phi}, \dot{J})$ which correspond to motion on circles $(\dot{\phi} = 0)$ and *action-angle-angle* flows $(\dot{I}, \dot{\phi}, \dot{\theta})$ which correspond to motion on the surface of tori (see figure 7 for definitions of (I, ϕ, θ).

The flow (3.4) in our apparatus at angle $\alpha = 0°$ is regular, and is of the action-angle-angle type as exemplified by figure 8 by means of an experimental Poincaré section. Upon perturbation the flow becomes

$$\left. \begin{array}{l} \mathrm{d}I/\mathrm{d}t = \alpha f_I(I, \phi, \theta, \alpha), \\ \mathrm{d}\phi/\mathrm{d}t = \Omega_\phi(I) + \alpha f_\phi(I, \phi, \phi, \alpha), \\ \mathrm{d}\theta/\mathrm{d}t = \Omega_\theta(I) + \alpha f_\theta(I, \phi, \theta, \alpha), \end{array} \right\} \tag{3.6}$$

where Ω_θ, and Ω_ϕ are frequencies of rotation in the direction of θ and ϕ, respectively, as defined above, and α is a small parameter (the angle of the impeller in the experimental system considered here). The distinguished invariant surfaces in the flow for $\alpha = 0°$ are the tori $I = $ constant as mentioned above. The existence of such surfaces for $\alpha \neq 0°$ depends on whether the ratio

$$f(I) = \frac{\Omega_\phi(I)}{\Omega_\theta(I)} \tag{3.7}$$

is sufficiently irrational. The KAM theory (Arnold 1978) in the context of three-dimensional steady flows, as developed by Moser (1968) and Cheng & Sun (1990) can be used to show that the unperturbed torus I persists in the perturbed case if $f(I) = \Omega_\phi(I)/\Omega_\theta(I)$ is sufficiently irrational in the sense that it satisfies the
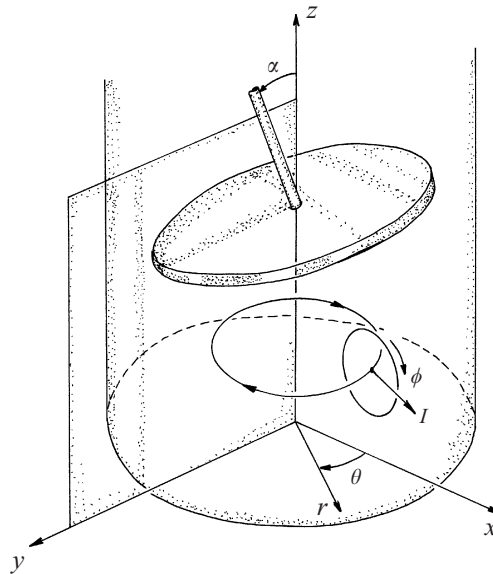
FIGURE 7. Coordinate system used in this study.

Diophantine condition

$$\frac{\Omega_\phi(I)}{\Omega_\theta(I)} - \frac{l}{k} \geqslant \frac{c}{k^\mu} \tag{3.8}$$

for $\mu > 2$ and for all integers k, l. Thus, tori for which the ratio of frequencies is sufficiently irrational and which satisfy the condition of (3.8) could survive. We say 'could' as it is impossible to say, from the current state of the theory of KAM-type for three-dimensional flows, whether a particular torus will survive – but it is possible to say that a majority of them will (see the extended discussion of this in Mezić & Wiggins 1994). On the other hand, if the ratio of the frequencies $f(I)$ is rational, the corresponding torus breaks into a higher-order torus (see for example figure 6c) surrounded by heteroclinic tangles. A schematic representation of this structure (the original reference is Arnold 1963, figure 6) is shown in figure 9, the number of islands being determined by the denominator of f (the reader is encouraged to look ahead to figure 13). The breaking of the torus is described by the Poincaré–Birkhoff theorem (Lichtenberg & Lieberman 1992). In the Poincaré section the unperturbed rational torus is composed of points all of which are periodic with a period equal to the denominator of f, say p. Perturbation results in the survival of just $2p$ periodic points, half of which are *elliptic* and half *hyperbolic* in character. Each elliptic point is surrounded by KAM curves, which correspond to the islands in the Poincaré section, and the hyperbolic points are the source of heteroclinic manifolds which cause chaotic motion. A perspective three-dimensional view of this structure is given in the review article by Helleman (1986).

The situation is different in the case when the tank rotates in the direction opposite to the disk rotation. Let us again discuss the case $\alpha = 0°$. The frequency Ω_θ, which is positive at the centre of the toroidal region, becomes negative at the walls due to the fact that the tank rotates in the direction that is opposite to the rotation of the disk. As the frequency Ω_θ changes continuously, there must be a toroidal surface I_r on which $\Omega_\theta(I_r) = 0$. In this case the flow (3.4) can locally (around the toroidal surface
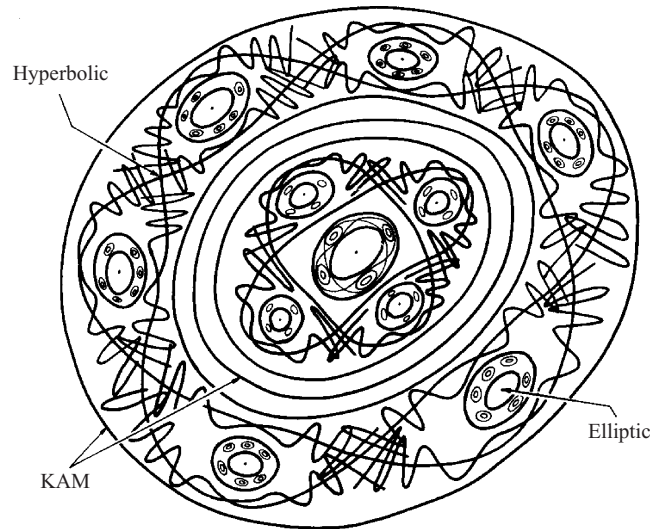
FIGURE 9. General picture of a near-integrable system showing the breakup of the most rational tori. Sufficiently irrational tori survive.

I_r) be written as an action-action-angle flow, which has the same form as (3.6) with $\Omega_\theta = 0$. It was first observed by Piro & Feingold (1988) on the basis of numerical computation and formal expansions that no invariant manifolds persist in this case and thus it allows global transport. Mezić (1999) discusses further the possibility of global transport (i.e. complete mixing), in this case related to the existence of pairs of saddle-foci fixed points, revealing a new mechanism of transport in three-dimensional flows quite different from the ones found in two dimensions. Unfortunately, while we can attribute the existence of global transport to this mechanism, we are incapable of visualizing the saddle-foci pairs in this experiment as they are localized around the surface I_r. On the other hand, the positive conclusion is that frequency analysis allows us to predict a mixing phenomenon – in this case global mixing – in our flow and suggests that this will happen even when the perturbation from the axisymmetric case (i.e. the angle α) is very small. This conclusion is amply supported by experiments.

Let us consider now what happens when Re becomes large. We would argue (as in Mezić 1994, introduction, Yannacopoulos *et al.* 1998 and Mezić 1998) that as the flow approaches an Euler flow with increasing Reynolds number, dynamical symmetries are introduced in the system which override geometrical asymmetries ($\alpha > 0°$ in our case) and the flow may become regular. This is a consequence of Arnold's (1978, Appendix 2, Theorem 11) theorem which states that bounded, steady Euler flows are regular, and we briefly review this below. The case of two-dimensional, unsteady Navier–Stokes flows has been rigorously treated in Balasuriya, Jones & Sandstede (1998).

Steady, isochoric, inviscid flow is described by

$$\rho(v \times \omega) = \nabla\zeta, \tag{3.9}$$

where $\omega = \nabla \times v$ is the vorticity and ζ a potential given by $\zeta = P + \rho v^2/2 + \rho g h$, with P being the pressure, $v = |v|$, ρ the density, g the acceleration due to gravity, and h the height above an arbitrary datum level.

Let us note a few implications of equation (3.9). In general, $\zeta = \zeta(x)$, and the surface defined by $\zeta(x) = $ constant – with normal $\nabla\zeta$ – is called a *Bernoulli* surface. Both v and ω are tangent to Bernoulli surfaces. This is so since $v \cdot (v \times \omega) = v \cdot \nabla\zeta \equiv 0$

and $\boldsymbol{\omega}\cdot(\boldsymbol{v}\times\boldsymbol{\omega}) = \boldsymbol{\omega}\cdot\nabla\zeta \equiv 0$. It is therefore convenient to think of the Bernoulli surfaces as streamsurfaces. Alternatively, since $\boldsymbol{v}\cdot\nabla\zeta \equiv 0$ it then follows that $\mathrm{D}\zeta/\mathrm{D}t \equiv 0$ and that ζ is constant over streamlines (and also pathlines and streaklines).

Before retaking the most general case consider the special situation corresponding to ζ being uniform (i.e. $\zeta \neq \zeta(\boldsymbol{x})$; note that a trivial case corresponds to $\boldsymbol{\omega} \equiv \boldsymbol{0}$). In general this implies that $\boldsymbol{v} \times \boldsymbol{\omega} \equiv \boldsymbol{0}$ and therefore the velocity and vorticity are co-linear at every $\boldsymbol{x}$, i.e. $\boldsymbol{\omega} = \beta(\boldsymbol{x})\boldsymbol{v}$, where $\beta(\boldsymbol{x})$ is some scalar function. This is called a Beltrami flow. Furthermore, since $\nabla\cdot\boldsymbol{\omega} = 0$ and $\nabla\cdot\boldsymbol{v} = 0$ we have $\boldsymbol{v}\cdot\nabla\beta = 0$ and the streamlines are constrained to belong to surfaces $\beta(\boldsymbol{x}) = $ constant, which act as a constant of the motion. However, if β happens to be uniform, i.e. $\beta \neq \beta(\boldsymbol{x})$, this constraint disappears and $\boldsymbol{v}(\boldsymbol{x})$ is not constrained to belong to any surface. Arnold conjectured that such flows, called strong Beltrami flows, may have complex topology; this was the suggestion taken up by Hénon and alluded to in §1. The ABC flows are an example of this class of flows. Potential flows ($\boldsymbol{\omega} = \boldsymbol{0}$) also do not constrain the velocity to lie on surfaces, and may be chaotic.

Due to non-genericity of the condition that velocity and vorticity are parallel, we argue that it is unlikely that with increase of Reynolds number the flow becomes Beltrami. Thus, consider further the implications of both $\boldsymbol{v}$ and $\boldsymbol{\omega}$ being tangent to the Bernoulli surfaces (Arnold 1978). Both streamlines and vortex lines lie on Bernouli surfaces. They can be formally obtained by the *diffeomorphisms* or *flows* $\boldsymbol{x} = \boldsymbol{f}_t\boldsymbol{x}_0$ and $\boldsymbol{x} = \boldsymbol{h}_t\boldsymbol{x}_0$, where t parameterizes the distance along the streamline or vortex line and $\boldsymbol{x}_0$ is the position at $t = 0$ (for simplicity the parentheses are omitted in $\boldsymbol{x} = \boldsymbol{f}_t(\boldsymbol{x}_0)$ and $\boldsymbol{x} = \boldsymbol{h}_t(\boldsymbol{x}_0)$). The vorticity equation

$$\boldsymbol{v}\cdot\nabla\boldsymbol{\omega} - \boldsymbol{\omega}\cdot\nabla\boldsymbol{v} = 0 \tag{3.10}$$

yields further details of the flow structure. Taking a scalar product of equation (3.10) with $\nabla\varphi$, for any $\varphi(\boldsymbol{x})$, yields

$$(\boldsymbol{v}\cdot\nabla)(\boldsymbol{\omega}\cdot\nabla)\varphi \cdot (\boldsymbol{\omega}\cdot\nabla)(\boldsymbol{v}\cdot\nabla)\varphi = 0. \tag{3.11}$$

Equation (3.11) can be written in terms of the *Lie bracket* [...] for the vector fields $\boldsymbol{v}, \boldsymbol{\omega}$ which is defined as

$$\mathrm{L}_v\mathrm{L}_{\omega\varphi} - \mathrm{L}_\omega\mathrm{L}_{v\varphi} = [\boldsymbol{\omega}, \boldsymbol{v}]\varphi = 0 \tag{3.12}$$

where the linear operators $\mathrm{L}_v, \mathrm{L}_\omega$ are given by

$$\mathrm{L}_v\varphi(\boldsymbol{x}) = \boldsymbol{v}\cdot\nabla\varphi = \left.\frac{\mathrm{d}}{\mathrm{d}t}\right|_{t=0}\varphi(\boldsymbol{f}_t\boldsymbol{x}) \tag{3.13}$$

and

$$\mathrm{L}_\omega\varphi(\boldsymbol{x}) = \boldsymbol{\omega}\cdot\nabla\varphi = \left.\frac{\mathrm{d}}{\mathrm{d}t}\right|_{t=0}\varphi(\boldsymbol{h}_t\boldsymbol{x}). \tag{3.14}$$

The operator L_v is simply the time rate of change along a streamline at position $\boldsymbol{x}$ (which is the material derivative since the flow is steady), and L_ω is similarly the time rate of change along a vortex line.

If the Lie bracket of two linearly independent vector fields is zero, as in (3.12), then the corresponding flows *commute*, that is $\boldsymbol{f}_t\boldsymbol{h}_s\boldsymbol{x} = \boldsymbol{h}_s\boldsymbol{f}_t\boldsymbol{x}$. This is easily seen from

$$\left.\frac{\partial}{\partial s}\right|_{s=0}\left.\frac{\partial}{\partial t}\right|_{t=0}(\varphi(\boldsymbol{h}_s\boldsymbol{f}_t\boldsymbol{x}) - \varphi(\boldsymbol{f}_t\boldsymbol{h}_s\boldsymbol{x})) = \mathrm{L}_v\mathrm{L}_\omega\varphi(\boldsymbol{x}) - \mathrm{L}_\omega\mathrm{L}_v\varphi(\boldsymbol{x}) = 0, \tag{3.15}$$

which is obtained using the definitions of the linear operators. This property has a direct bearing on the topology of the Bernoulli surfaces. If the Bernoulli surface is

compact, connected and differentiable and if the pair of vector fields (v, ω) tangent to the surface is linearly independent with $[v, \omega] = 0$, then the surface is topologically equivalent to a torus (Arnold 1978).

The above result implies that for bounded, inviscid, incompressible flows which have $v \times \omega \neq 0$ everywhere in the domain, the streamsurfaces (Bernoulli surfaces) are either deformed tori or cylinders. Every streamline (pathline) on the tori either wraps around and densely fills the surface (quasi-periodic streamline) or is closes onto itself (periodic). Every streamline on the cylinder is closed. Thus the flow is everywhere regular and there is no chaotic motion. This issue is considered further at the end of the paper. Before abandoning theoretical considerations we should mention an alternative way to analyse these types of flows.

A method for global qualitative analysis of the flow was suggested by MacKay (1994) in terms of the stable and unstable manifolds of the flow. This approach does not require the flow to have a Hamiltonian structure but does require an insight into the basic flow pattern. The method involves the identification of the hyperbolic fixed points in the flow (stagnation points) and the consideration of the interaction of the heteroclinic manifolds of the different fixed points. A sketch of the flow skeleton based on these ideas is presented in §5.

4. Numerical results

The system was modelled numerically using the computational fluid dynamics (CFD) software package FIDAP® v7.52 from Fluent. Once the velocity field was determined, particle tracking was performed both with FIDAP® and HyperTrace® from Cray (Silicon Graphics). Additional custom code was written to perform various additional analysis including modifications to the FIDAP® particle advection source code to perform stretching and deformation calculations.

FIDAP® uses a finite element method to solve the Navier–Stokes equation. The tank was modelled completely since the impeller angle is used as a means of destroying symmetry. The simulation was run as a steady, laminar, Newtonian, isothermal problem using the segregated solver and a mixed, discontinuous pressure condition. The top free surface was modelled as a zero-flux boundary ($v_z = 0$). For moderate Reynolds numbers, this is a good assumption (experimentally, at $N_I = 300 \,\text{RPM}$, $Re_I = 65$, the deformation in the top surface was less than $1 \,\text{cm}$ deep). A further simplification was the elimination of the impeller shaft from the simulation. This primarily reduced difficulties due to deformation of the grid. Since the focus was on the flow below the impeller it was anticipated that this would have minimal effect. Upon comparison between the experimental and numerical Poincaré sections, the assumption appears to be reasonable.

A staged approach was used to facilitate convergence accuracy and reduce computational time. Three grids were used with an increasing number of nodes (26 094, 132 730, and 385 648 respectively). Each successive grid was used as the initial condition for the next. All grids were constructed with 27-node brick elements with triquadratic interpolation. A fourth intermediate grid (second highest nodal density) was used periodically as part of grid convergence verification. While the initial two grids are symmetric, having an equal number of nodes both above and below the impeller, the final grid concentrates nodes below the impeller. This does not result in significant differences in the velocity field, but rather, serves to facilitate the accuracy of the interpolation and integration scheme built into FIDAP® for particle tracking. The final grid can be seen in figure 10.
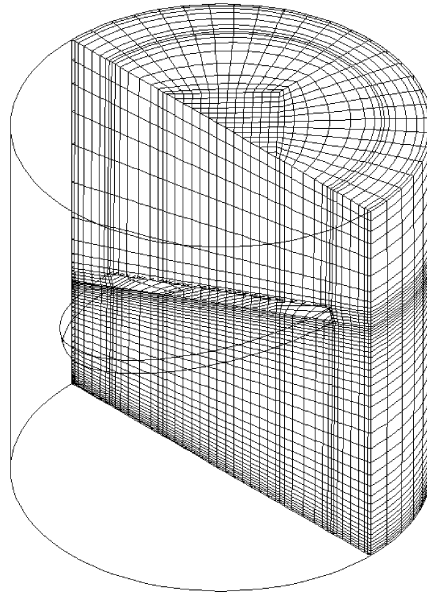
FIGURE 10. Final numerical grid. A total of 385 648 nodes with 27-node quadratic elements. The grid is biased with 78% of the nodes below the impeller to facilitate particle tracking. An unbiased (50 : 50) grid with 310 k nodes was used to ensure the velocity field result was not affected.

The simulations were performed on a Silicon Graphics Indigo2 workstation with 384 MB of RAM. The processor is a 200 MHz R4400 with a SpecINT95 rating of 3.5 and a SpecFP95 rating of 3.0 (Spec95 data obtained internally from SGI). Each grid solution was run to a relative velocity error of 10^{-8} before proceeding to the next refinement. All grids were run within main memory with the fine grid requiring 351 MB of RAM. Properly staged, convergence times for the 30 RPM, $\alpha = 0°$ case are 8 hours, 24 hours, and 96 hours respectively. Without the staged approach, attempting the final grid directly can easily take in excess of two weeks (for this parameter set).

4.1. *Comparison to PIV results*

The results of the velocity field calculations are consistent with those obtained from the PIV experiments as can be seen in figure 11. The location of the recirculation region agrees well. There are differences in the discharge region of the impeller, but this is also the region of highest difficulty for the PIV measurements (due to the strong out-of-plane motion). We know from the dye advection studies that there is a sharp separation line from the impeller to the tank wall (no dye passes into the region above the impeller). Investigation of the $v_z = 0$ line in the simulation agrees with this no-flux observation.

4.2. *Advection analysis*

Particle tracking for advection studies was performed both in FIDAP® and, as a cross-check, HyperTrace® (for Poincaré sections). FIDAP® uses a second-order Eulerian integration scheme to match the quadratic nature of the elements. A variety of error controls and time step limits were used, although it was found that for a given grid, the integrations were fairly robust, but the surfaces of the regular tori were somewhat
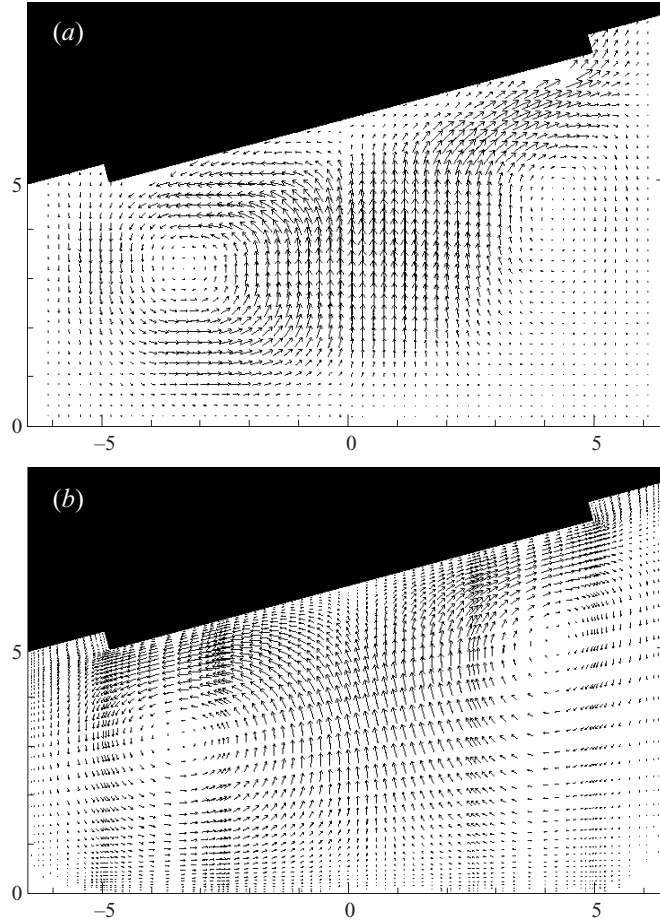
FIGURE 11. Comparison of (*a*) experimental (PIV) and (*b*) numerical (FIDAP®) velocity fields ($\alpha = 15°$, $N_I = 30$ RPM, $N_T = 0$ RPM, $Re_I = 6.5$).

noisy and in some cases unstable. Adding additional nodes into the region improved the advection substantially, although as already mentioned, did not significantly alter the velocity field.

The particle trajectories were then used to calculate circulation times and Poincaré sections. Code which would determine the intersection locations and times for arbitrary xyz cut planes in the system was used. For the Poincaré sections and Ω_0 frequencies, this was simply the $x = 0$ plane. For the Ω_ϕ frequencies, the centre of the recirculation region was first determined by locating the $v_r = v_z = 0$ point. The height of this centre was designated z_{circ} and the crossings measured using the z_{circ}-plane.

From figure 12, it can be seen that the agreement between the numerical Poincaré sections and the experimental dye advection studies is very good. We have accurate matching between the period-4, period-5, and period-6 tori. The last is faint in the photograph, but can be picked up with careful observation, or by using image analysis. Here, the simulated advection time for the trajectories in the regular islands is 60 minutes. It should be noted that considerable care must be taken in advection simulations. While the trajectories shown agree with the experiments, other orbits explored occasionally did not satisfy continuity constraints (they spiralled onto a stable
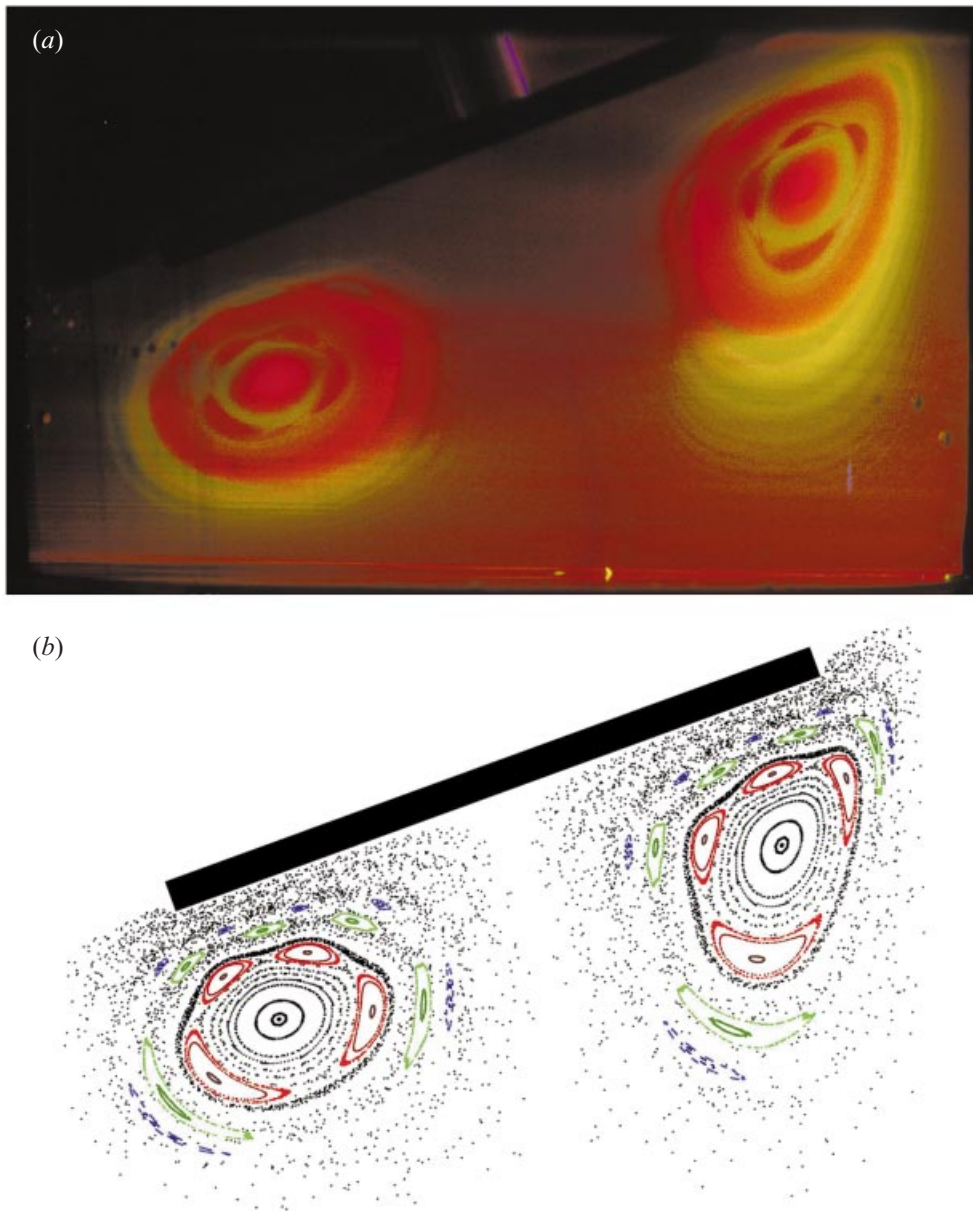
FIGURE 12. Comparison of (*a*) experimental and (*b*) numerical Poincaré sections ($\alpha = 20°$, $N_I = 30$ RPM, $N_T = 0$ RPM, $Re_I = 6.5$). There is a good match between the position and number of the different toroidal chains. The red (period-4) and green (period-5) are easy to match. Closer inspection shows matching of the blue (period-6) islands as well. The experimental photo was taken more than seven hours after needle removal.

surface). This problem can be exacerbated by poor grid design or poor convergence. The reader is directed to Souvaliotis, Jana & Ottino (1995) for a discussion of these issues.

The calculation of the ratio of frequencies, $f(I)$, for the unperturbed flow ($\alpha = 0°$, figure 13) proceeds in the same manner. As is clear from figure 8, the structure formed
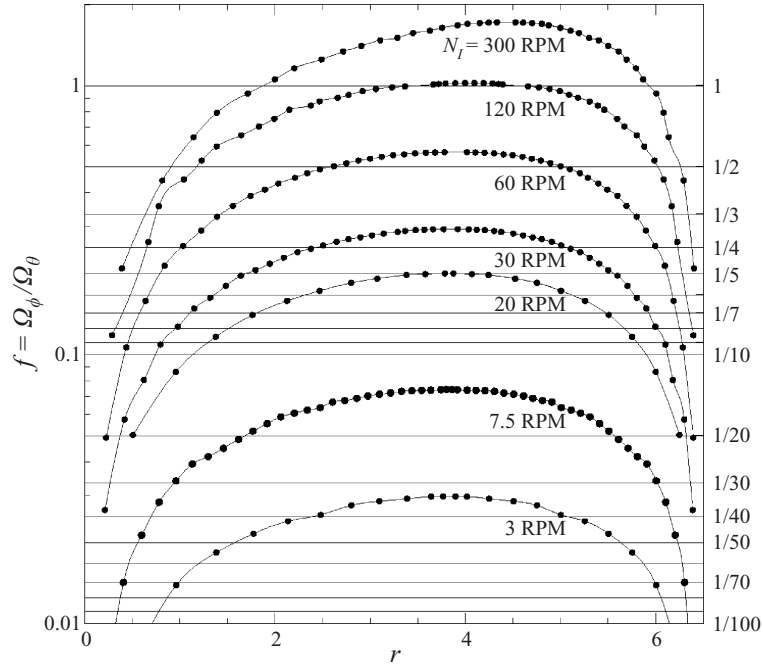
FIGURE 13. Ratio of frequencies of rotation for $\alpha = 0°$ at differing impeller speeds ($3 < N_I < 300$ RPM, $0.6 < Re_I < 65$) as a function of distance from the centreline of the vessel.

by the flow is a deformed torus and the action in this case is given by

$$I = \frac{1}{2\pi} \int_0^{2\pi} R(\phi) \, d\phi,$$

where $R(\phi)$ is the radius of the curve corresponding to the deformed torus in the Poincaré section measured from the centre of transverse rotation. The times between intersections of a trajectory with a horizontal surface, $z = $ constant, passing through the centre of rotation of the torus (z_{circ}-plane), are used to determine the average recirculation time in the ϕ-direction (τ_ϕ). Similarly, intersections with a vertical plane passing through the tank axis are used to find the average recirculation time in the θ-direction (τ_θ). The ratio of the frequencies in the action-angle coordinates is then calculated as $f = \Omega_\phi/\Omega_\theta = \tau_\theta/\tau_\phi$. This is performed for many points spaced from the centre of the recirculation region out to the tank wall. The trajectory is then checked to find the inner radius (which corresponds to a unique action I), and the results tabulated in terms of the inner and outer radial positions measured from the tank axis rather than the action. This is repeated for a wide range of impeller rotation rates.

5. Experimental results

Figure 14 shows the evolution of the dye structure during a typical experiment. Sequential injection of the different coloured dyes reveals an increasing extent of the underlying flow structure. When all the dye injection needles are removed from the tank, the dye structures relax to their undisturbed equilibrium positions as shown in §2.9. Experiments show that the disturbance due to the needles is the greatest at the lowest Reynolds number. This is because at low Reynolds numbers the disturbance
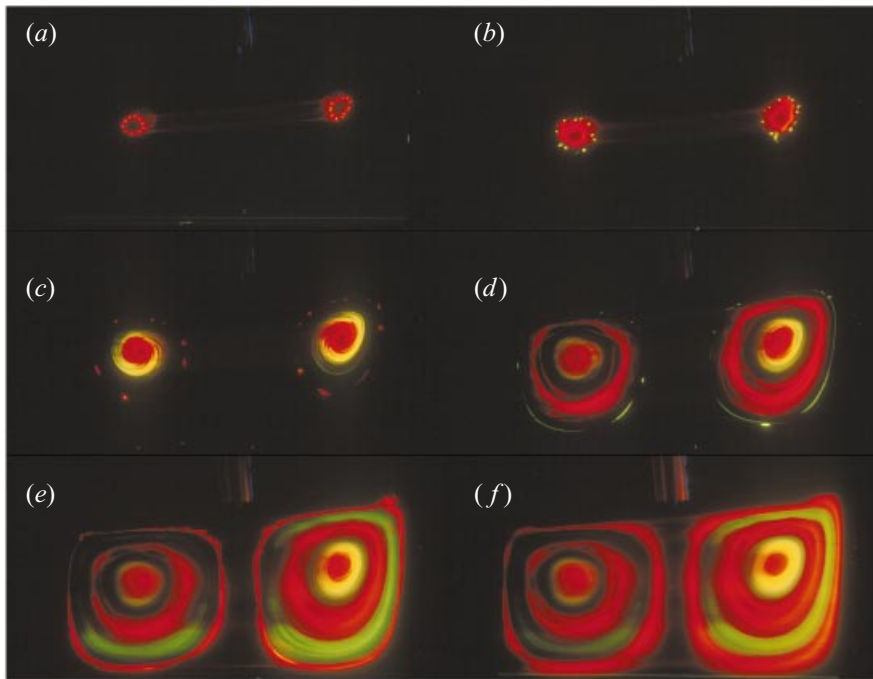
FIGURE 14. Photo sequence ($\alpha = 5°$, $N_I = 30$ RPM, $N_T = 0$ RPM, $Re_I = 6.5$) showing the buildup of the dye layers. There are a total of five injections starting at the innermost red layer (*a*), progressing through (*b*) yellow, (*c*) red, (*d*) green, and finally a red layer (*e*). The final relaxed state is shown in (*f*).

due to the needle decays very slowly ($\sim 1/r$) while at high Reynolds numbers the disturbance is confined to a thin wake region behind the needle. The equilibrium structure produced after all the needles are removed is, however, invariant and the basic features remain unchanged even after more than 7 h of operation (figure 12*a*).

Streaklines produced by dye injection are coincident with pathlines in the case of a steady flow, as used in the present study. Thus the experimental surface of section, which is the intersection of the streaklines with the sheet of laser light, is by definition a Poincaré section for the flow. In addition, the unperturbed flow ($\alpha = 0°$) is rotationally symmetric so that the Poincaré section obtained can be analysed by the theory for two-dimensional mappings over most of the flow region, as mentioned in §3. Figure 12 shows the Poincaré sections obtained by means of experiments and computations. The basic structure of the flow, comprising islands of regular flow surrounded by regions of chaotic flow, is visualized more easily in such Poincaré sections for three-dimensional flows than for two-dimensional flow experiments. For example, KAM tori (invariant toroidal surfaces which survive the perturbation from axisymmetry) appear as closed curves (regular islands) in the Poincaré section (figure 5), and higher-order tori (tubes which wind around the tank several times before joining to form a closed surface) appear as island chains (figure 6*b*, *c*). Experimental visualization of islands, and in particular higher-order islands, is difficult in two-dimensional flows. Even in numerically obtained Poincaré sections it typically takes thousands of periods to define the contour of an island. In contrast, islands in the experimentally determined Poincaré sections for the three-dimensional flow shown here become visible on the order of 10^1 to 10^2 circulation times. The robustness of
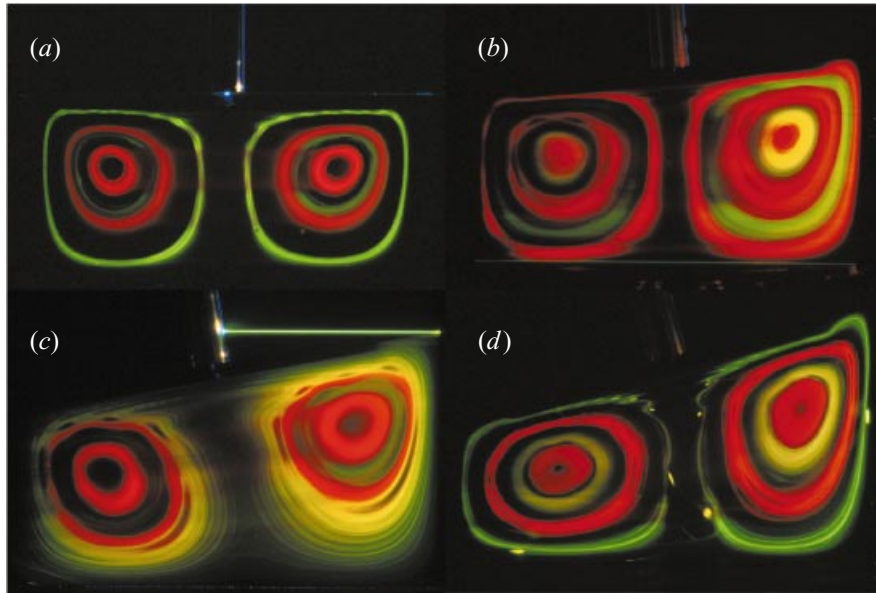
FIGURE 15. Variation of impeller angle at fixed impeller speed ($N_I = 30$ RPM) and no tank motion ($N_T = 0$ RPM). (a) $\alpha = 0°$. (b) $\alpha = 5°$. (c) $\alpha = 10°$. (d) $\alpha = 15°$.

the experiments lies in the constant dye injection and the obvious fact that fluids are continuous and not discrete. This produces connected structures as opposed to the peppered-like appearance of computational results involving the tracking of single particles (figure 12). An experimental streakline on a torus is stretched into a ribbon along the surface of the torus; thus the entire island is revealed in a few circulations. In chaotic regions a streakline is stretched into a sheet and folded, repeatedly, showing typical striated patterns in a two-dimensional cut.

The experimental surface of section shows nested tori which survive the perturbation, and tori with rational winding numbers break up into island chains surrounded by chaotic layers. The outermost torus is surrounded by a chaotic sea. The flow structure visualized by the dye can be understood in the context of the theory outlined in §3. Notice that the area of every island in the chain is not the same, implying that the experimental Poincaré section is not the result of an area-preserving mapping. This is because the azimuthal velocity varies with cross-sectional position. The velocity field must be transformed to get it in the form given in equation (3.4). We present below an analysis of the structure and how it is modified by change in the system parameters: impeller angle, tank rotational speed and impeller rotational speed.

Effect of impeller angle

Figure 15 shows the equilibrium dye structures obtained for increasing values of the impeller angle for a fixed impeller speed ($N_I = 30$ RPM) and no tank rotation. The unperturbed flow ($\alpha = 0°$) shows axisymmetric nested tori (figures 8, 15a) as expected from equation (3.6). The computed ratio of the rotational frequencies ($\Omega_\phi/\Omega_\theta$) as a function of the position of the toroidal surface is shown in figure 13. The ratio of frequencies f does not exceed any rational numbers with denominators 2 and 3. The frequency ratio $\frac{1}{4}$ is obtained for the torus with outer surface distance $r_o = 5.1$ cm from the axis of the tank and inner radius $r_i = 2.5$ cm. Theory discussed earlier indicates that this torus is most likely to break upon perturbation into a four-fold

torus surrounded by a chaotic layer. In the surface of section, the four-fold torus would appear as two chains of four regular islands, one for each side of the torus, each island chain surrounded by a chaotic layer (in fact, all the tori with rational frequencies break; however, because of the coarseness of dye visualization, only those islands with smallest denominator frequency are large enough to be visible for the smallest perturbations). With increasing perturbation the next torus whose breakup becomes visible ($r_i = 1.7\,\text{cm}$, $r_o = 5.6\,\text{cm}$) would form a chain of five islands and the following one ($r_i = 1.3\,\text{cm}$, $r_o = 5.8\,\text{cm}$) would form a chain of six islands. This sequence would continue with increasing perturbation, until the theory is no longer valid because the perturbation is not small.

Applying a small perturbation to this system ($\alpha = 5°$) has little overall effect. Most of the regular tori are preserved (to the resolution of the experimental visualization) and the main effect is to distort the tori to slightly asymmetric shapes. A small qualitative change that is, however, significant from the viewpoint of analysis is the appearance of a four-island chain at $r_i = 2.3\,\text{cm}$, $r_o = 5.3\,\text{cm}$. The radial distance is measured in the left quadrant, which appears to be less distorted than the right quadrant from the unperturbed structure. The distances are also measured along a line joining the centres of the innermost islands from the midpoint of the line. There is good agreement between the experimental location of the island chain and that predicted from theory.

Increasing the impeller angle to $\alpha = 10°$ (figure 15c) has the effect of significantly distorting the tori into asymmetric shapes. In addition, the region outside the outer-most torus becomes chaotic. A period-5 island chain is clearly visible at this impeller angle in addition to the period-4 island chain. The location of the period-5 island ($r_i = 1.5\,\text{cm}$, $r_o = 5.8\,\text{cm}$) is again in good agreement with the predictions of the theory in spite of the relatively large distortion of the tori. Further increase in the impeller angle to $\alpha = 15°$ results in greater distortion of the tori and the size of the chaotic region increases. A period-6 island chain is now visible at $r_i = 1.1\,\text{cm}$ and $r_o = 5.5\,\text{cm}$, in reasonable agreement with theory.

The source of the chaotic sea beyond the outermost torus is the heteroclinic behaviour of the stable and unstable manifolds initially along the central axis. A perspective view of a streakline in this region is shown in figure 16(a). The unstable manifold is visualized experimentally by dye injection close to the tank wall (figure 16b). The dye tube envelops the unstable manifold and traces its path upward along the central axis and then radially outward as shown in figure 16(b). The intersections of the dye envelope with the laser sheet are clearly visible. Decomposition of the flow into action-angle-angle variables breaks down in the central region near the manifolds since axial motion dominates and azimuthal rotation is small. Thus the flow in this region is truly three-dimensional since it cannot be reduced to a two-dimensional mapping as is possible for the toroidal flow regions. For $\alpha = 0°$, the unstable manifold from the hyperbolic point on the base joins smoothly with the stable manifold to the hyperbolic fixed point on the impeller. Upon perturbation the manifolds become separated as seen from the experiments. A schematic view of the skeleton of the flow is given in figure 17.

Effect of impeller rotational speed

The impeller rotational speed has an important effect on the flow and thus on the mixing in the system. At low impeller speeds the Reynolds number is small and thus the radial circulation, which is produced by centrifugal forces, is small. At high rotational speeds (corresponding to high Reynolds numbers), the flow near the impeller can be approximated by that of an infinite disk rotating in a fluid. In this
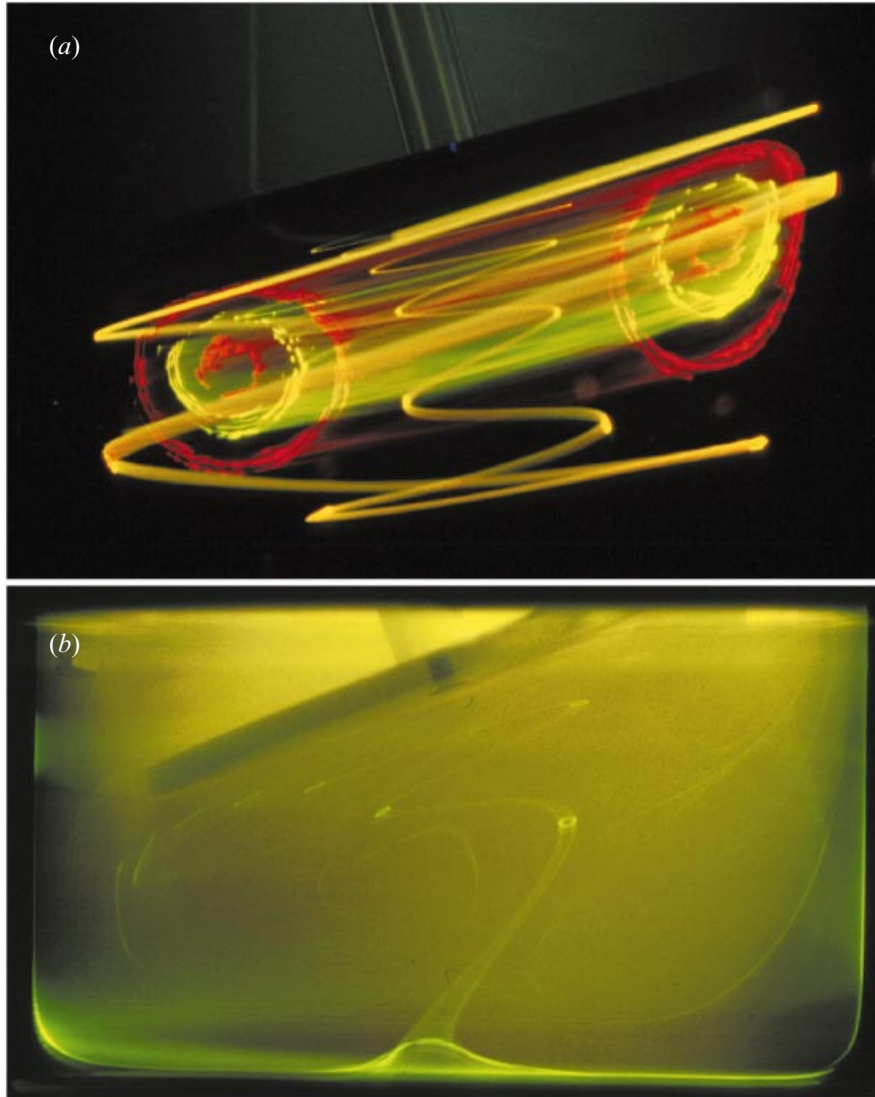
FIGURE 16. Visualization of an unstable manifold. (a) $\alpha = 15°$, $N_I = 15$ RPM, $N_T = 0$ RPM.
(b) $\alpha = 20°$, $N_I = 30$ RPM, $N_T = -3$ RPM.

case the radial volumetric circulation rate is estimated as (Batchelor 1967, p. 290)

$$Q \approx \pi R^2 (v N_I)^{1/2}, \tag{5.1}$$

where R is the radius of the disk and v is the kinematic viscosity of the fluid. The thickness of the boundary layer within which the radial flow is confined is

$$\delta \approx 6(v/N_I)^{1/2}. \tag{5.2}$$

Thus the circulation increases with rotational speed but the boundary layer thickness decreases. The graphs of the computed frequency ratio with position of the torus for $\alpha = 0°$, and for the different rotational speeds, shown in figure 13, confirm the above discussion: at low rotational speeds the ratios are low, implying a lower
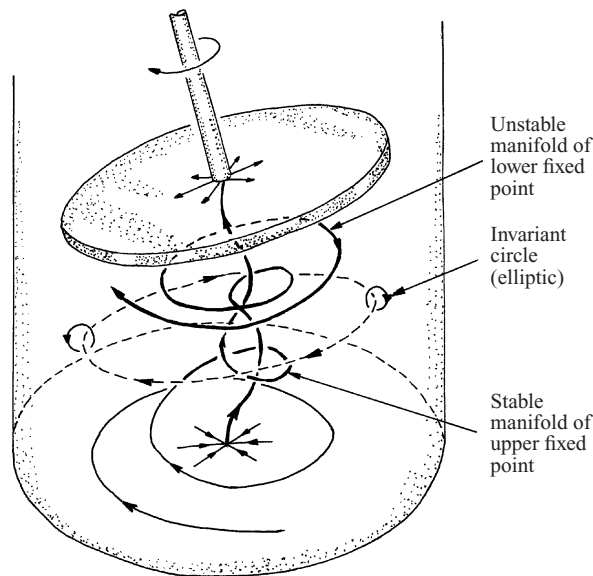
FIGURE 17. Schematic of trajectories.

radial circulation relative to the azimuthal circulation, and increase with increasing rotational speeds.

Figure 18 shows the experimental Poincaré sections obtained for the different rotational speeds. At the lowest rotational speed, the flow is entirely regular comprising nested tori which are distorted from the regular axisymmetric shape due to the relatively high impeller angle ($\alpha = 15°$) used (figure 18a). The ratio of frequencies indicates that there may exist island chains of period 40; however, such islands are probably too small to be visualized experimentally. Increasing the rotational speed to 20 RPM produces an island chain of period-6, which is as expected from theory (figure 13), and a small region of chaos near the axis. The next rotational speed studied (30 RPM) gives island chains of period four and five as seen previously (figure 15c), and the region of chaos becomes larger. Further increase in the rotational speed to 60 RPM results in a significant increase in the size of the chaotic region. However, tori survive even at this rotational speed. For this case the maximum of f is larger than $\frac{1}{2}$ (figure 13). Thus, we expect chains of two islands to appear, and this is observed experimentally (figure 18d). Period-4 and -5 chains of islands are visible on the periphery of the surviving tori.

In spite of the large perturbations the structure conforms to the theory, which predicts the formation of period-1, -2, -3, -4, -5 and higher-period island chains, and the analysis explains the results of figure 18 where increasing the impeller speed (and thus moving up with f in figure 13) decreases the number of islands in the most prominent chain.

The above results indicate that mixing (from the viewpoint of the size of the region of chaotic motion) improves with rotational speed over the range of speeds considered. Furthermore, increasing the speed reduces the time required for mixing for a given system. A study of the effects of increasing Reynolds number on mixing for slow flows was done by Bajer & Moffatt (1992). Our experiments confirm that increased inertia causes more chaos. Thus both results appear to support the practice of increasing speeds for faster mixing in a stirred tank. This is expected. However, even
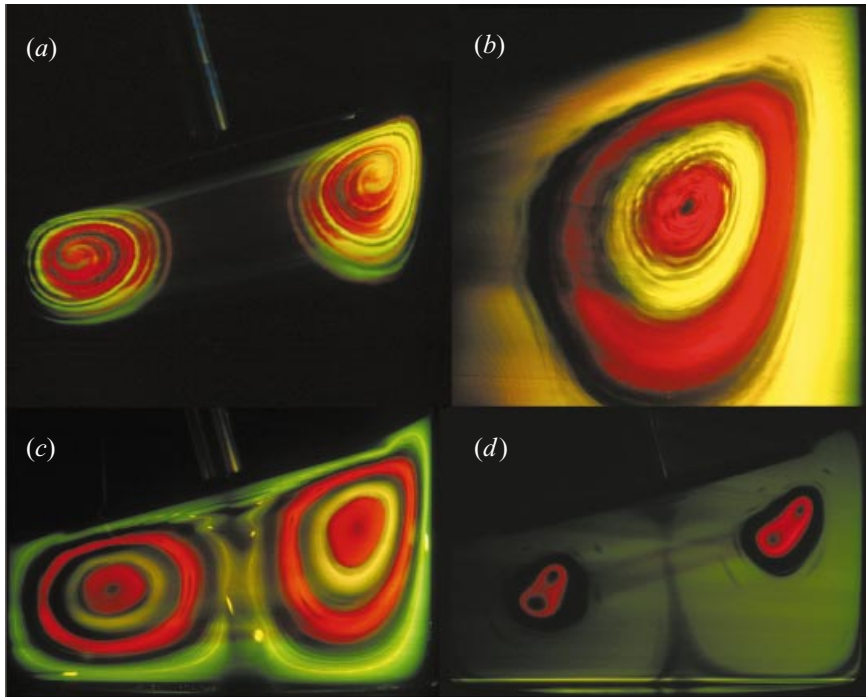
FIGURE 18. Variation of impeller speed at fixed angle and no tank motion ($N_T = 0$ RPM). (a) $N_I = 3$ RPM, note the strong residual effect from the needles. (b) $N_I = 20$ RPM, a high-period torus has formed along the inner edge of the outermost yellow region. This illustrates the high resolution of this technique. (c) $N_I = 30$ RPM, more (and larger) tori are beginning to form. (d) $N_I = 60$ RPM, much of the system is chaotic with three outer high-period tori (the dark regions). The inner region still has a strong regular behaviour.

higher RPM values should make the system closer to an Euler flow, and based on the theory outlined above and in Mezić (1994, introduction), Yannacopoulos *et al.* (1998) and Mezić (1998) one may speculate that the trend observed above should reverse. That is, the size of the chaotic region should reduce with increasing Reynolds number beyond a certain value. Transition to turbulence may, however, prevent experimental observation of this effect in this system.

Effect of tank rotation

Rotation of the tank at a constant angular speed in a direction opposite to that of the impeller is nearly equivalent to rotating the impeller at a higher speed when the impeller angle $\alpha = 0°$ (the inertial forces are higher in the latter case). However, for non-zero impeller angles the flow with tank rotation is qualitatively different from that without tank rotation since in the case with tank rotation when the frame of reference is fixed on the tank, the impeller appears to rotate about its axis and precess as well. The differences in the flow are reflected in the experimental surfaces of section (figure 19) which are dramatically different from the case for no tank rotation with the same impeller angle $\alpha > 0°$. The most noticeable difference is the widespread chaos in the system at even at low impeller angles and transport to the region above the impeller. At the low impeller angle ($\alpha = 5°$) a period-1 island is clearly visible. The island persists even at the higher angle ($\alpha = 20°$). The impact of chaos is dramatically
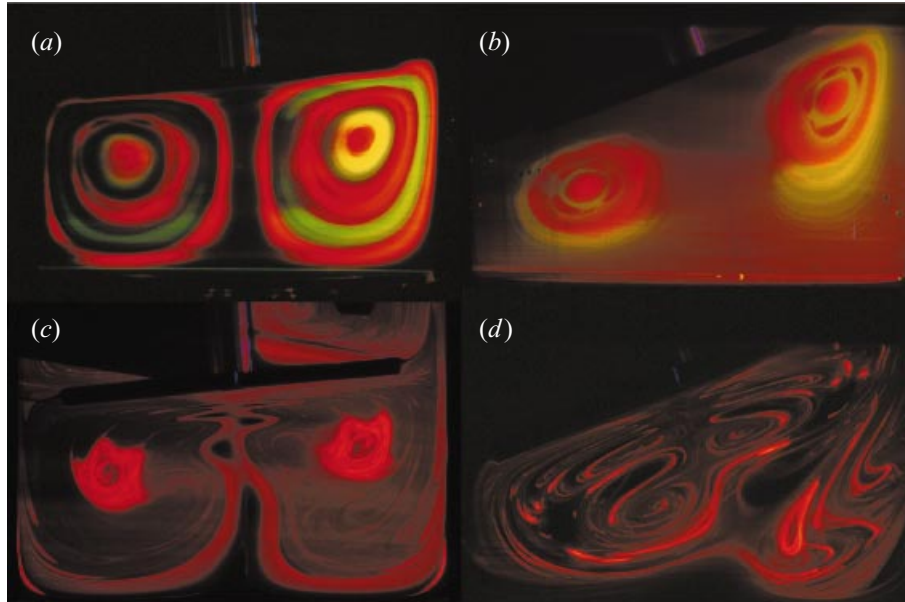
FIGURE 19. Effect of fixed tank speed ($N_T = -3$ RPM) on mixing for different impeller angles and fixed impeller speed ($N_I = 30$ RPM). (a, c) $\alpha = 5°$: (a) is without tank rotation, (c) is with rotation. (b, d) $\alpha = 20°$: (b) is without tank rotation, (d) is with rotation. Regarding efficiency, note that (b) is after approximately 7 hours of mixing while (d) is after 7 minutes.

apparent in the mixing times for the two cases: figure 19(b) is after 7 hours of mixing; figure 19(d) is after 7 minutes.

In practice the mixing ability of flows is often compared in terms of cross-sectional streamlines and circulation regions. This may be quite misleading. Figure 20 shows the computed streamlines for the transverse flow for the axisymmetric case ($\alpha = 0°$). While the transverse motion is toroidal as in the case with no tank rotation, the azimuthal flow has a plane of zero velocity ($v_\theta = 0$), shown as a line superimposed on the streamlines in figure 20. This reversal of flow is also depicted in figure 21. The action-angle-angle decomposition thus breaks down in two regions in the flow: near the axis and in the vicinity of the zero azimuthal velocity surface. Figure 22 shows a curve for the inverse of the ratio of rotational frequencies ($1/f$) for the axisymmetric case. The inverse ratio, $1/f$, goes to zero for the torus at $r_i = 0.05$ cm and $r_o = 6.45$ cm implying that there is no net azimuthal motion on the torus, and these orbits close after once going around in the ϕ-direction. When cast in action-angle variables, the motion on this torus is of the *action-action-angle* type (on circles of action I_r). Perturbation causes these circles to break in saddle node pairs as mentioned in § 3, and this is a source of chaos.

6. Conclusions and outlook

We have presented a bounded, three-dimensional flow system that allows the investigation of geometrical and dynamical chaotic mixing effects and lends itself to detailed experimental observation and high-precision computational inspection. The system mimics a stirred tank. However, the steady boundary conditions make it easy to model both numerically and theoretically. This sets it apart from tank flows with bladed impellers while still highlighting essential mixing mechanisms. The flow structure, cap-
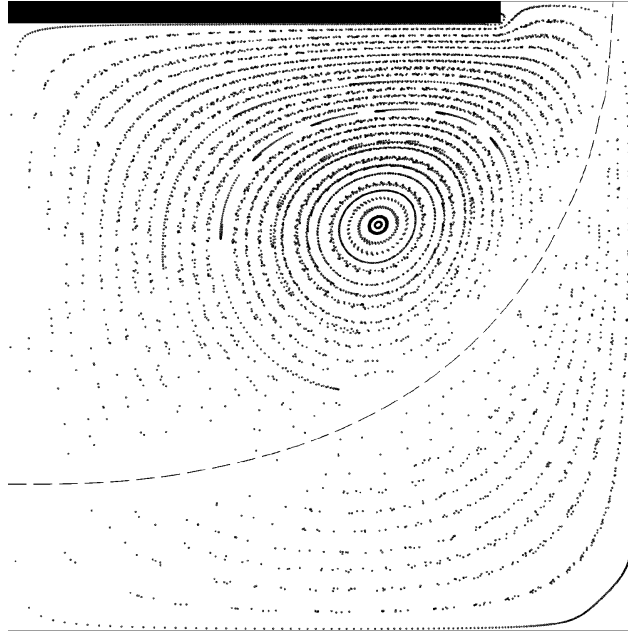
FIGURE 20. Poincaré section for $N_I = 30$ RPM, $N_T = -3$ RPM. Dashed line indicates cross-section of stagnation surface normal to the cut plane. Note the sparseness of the crossings near this line due to the low material flux in this region.
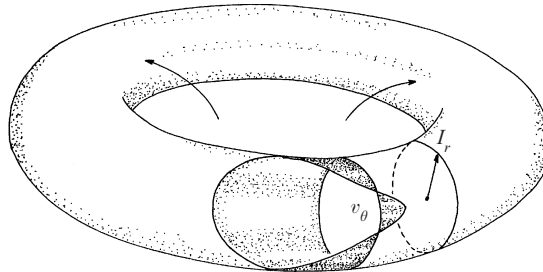

FIGURE 21. v_θ component in the counter-rotating flow for $\alpha = 0°$.

tured by means of cuts with a laser sheet (experimental Poincaré section), is visualized via continuously injected fluorescent dye streams and reveals detailed chaotic structures and chains of high-period islands. The experimental technique is robust and fine structures can be identified in relatively short times. Disturbance due to the injection needles is significant, especially at low *Re*, but equilibrated dye structures – after all needles are removed – are accurately visualized as is apparent from their invariance over long periods of mixing (24 h). The experimental technique can be used to map the skeleton of structures within the flow (significantly faster than numerically).

We find that increasing the impeller angle at a fixed rotational speed increases the size of the chaotic region. Increasing the rotational speed for a fixed impeller angle also increases chaos in the system. Increasing *Re* generally reduces the order of the tori formed, but this does not guarantee 'better' mixing.

Finite-element computations give a good description of the flow and PIV velocity vectors in a cross-section are in good agreement with the computed results. Most
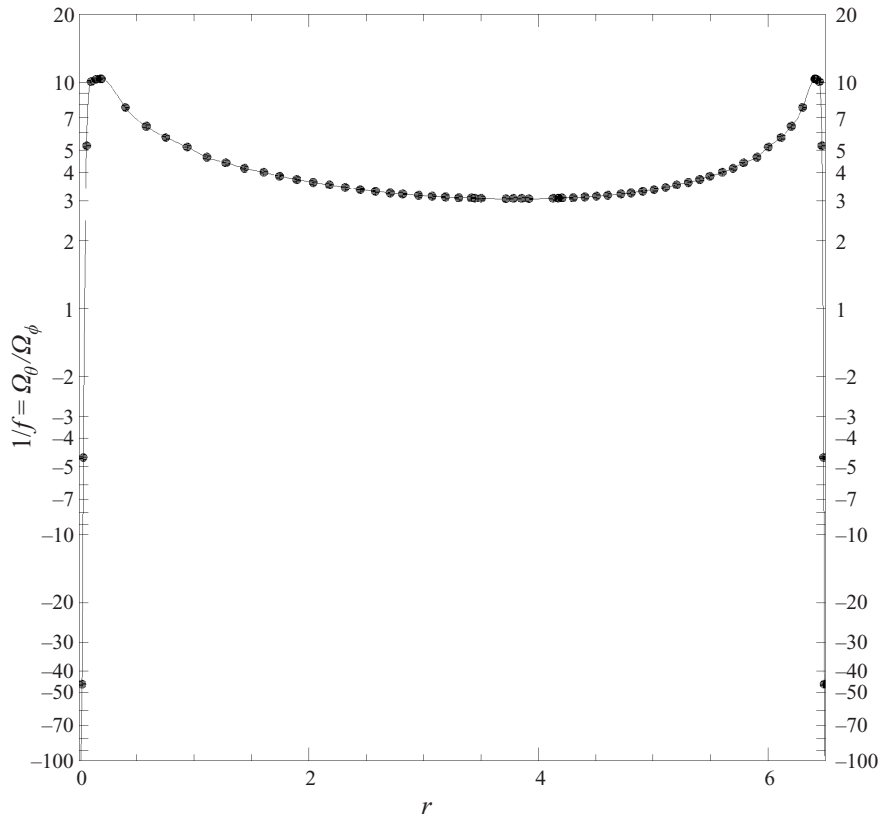
FIGURE 22. Ratios of frequencies of rotation for $\alpha = 0°$ in the counter-rotating case. $N_I = 30$ RPM, $N_T = -3$ RPM.

significantly, the computed Poincaré sections are also in good agreement with experimental sections; this is a more stringent test since it involves advection of particles over long times.

Predictions of existing theories for chaotic advection in three-dimensional volume-preserving flows were tested. The system is analysed by reducing the steady three-dimensional flow to a two-dimensional mapping, for which a large number of theoretical tools exist. The reduction, using the concept of action-angle-angle variables, is not uniformly valid and breaks down near the axis of the tank where the azimuthal frequency of rotation is small. In the region of validity of the theory, toroidal invariant surfaces are obtained as predicted by theory, and these surfaces break into higher-order tori upon increasing perturbation from axisymmetry. These higher-order tori are visualized as island chains in the Poincaré section. The ratio of two frequencies of particle motion – the frequency of motion around the vertical axis and the frequency of recirculation in the plane containing the axis – is identified as the crucial parameter. Computational predictions of the breaking of tori are in excellent agreement with experimental results. Most significantly, the same parameter allows the identification of operating conditions – counter-rotation – where small perturbations lead to nearly complete mixing. This suggests means of improving mixing in viscous flows: greater asymmetry and introducing regions of flow reversal (internal stagnation surfaces). Also, from a practical viewpoint, this would suggest that frequency analysis may
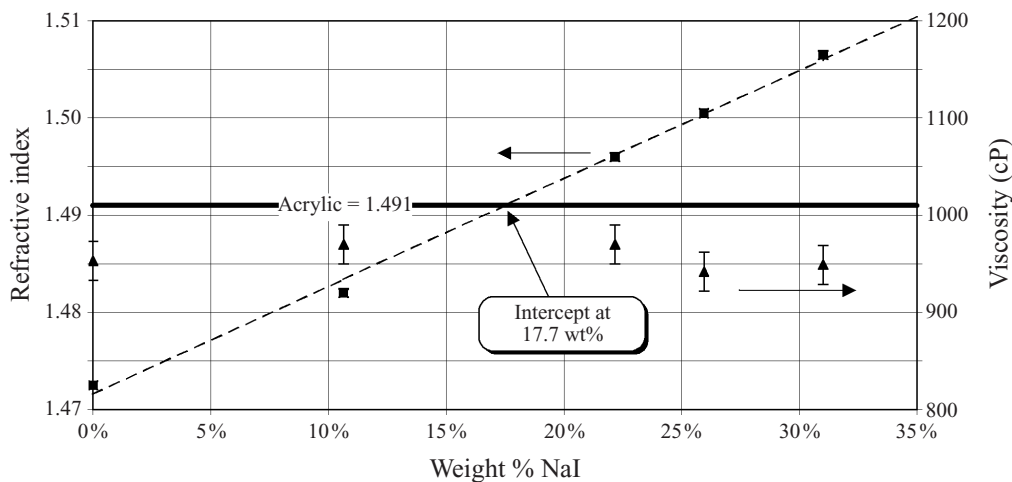
FIGURE 23. Optical density adjustment data. Addition of sodium iodide (NaI) to glycerine serves to increase the optical density. Square symbols represent the refractive index while the triangle symbols verify that the viscosity does not vary significantly. The refractive index of the vessel materials (acrylic) is shown by the solid horizontal line. Measurements at 22 °C.

be the logical next step beyond the popular 'turnover-time' correlations currently employed by industrial practitioners.

A few ideas about possible experimental extensions are presented here. As indicated earlier a full three-dimensional picture of structures within the flow should be possible using laser sheet scan and image analysis. More challenging are effects at high *Re*. As the Reynolds number increases, the flow approaches an inviscid flow – in regions away from solid boundaries – and the motion in these regions should become regular. Thus increasing the stirring rate (higher Reynolds number) may have the counter-intuitive effect of producing poorer mixing, as explained in Mezić (1994, introduction), Yannacopoulos *et al.* (1998) and Mezić (1998). Two factors that should be considered in addition are: (i) the flow may become turbulent, and (ii) some inviscid flow regions may also be regions of irrotational flow for which Arnold's analysis is not valid. An example of (ii) is the axisymmetric extensional flow along the centre of the mixing tank. There is no *a priori* reason why a steady irrotational flow could not be chaotic.

Unfortunately our device is limited to the range of Reynolds numbers that can be explored since at high speeds a vortex forms in the free surface. One could make the argument that the flow below the disk will remain relatively unaffected, but at some point it is inevitable that communication between the two regions will be significant. Our device however is unable to capture this. At 300 RPM we get about a 1 cm vortex; by 1000 RPM the vortex extends down, touching the impeller. Since we primarily only look in the region below the impeller, the 1 cm surface deflection has little effect on the observations in the lower half. However, the Reynolds number is not sufficiently large to verify the theory. The ideal device should therefore have a closed lid and a magnetically levitated disk (or any other shape) impeller or perhaps a sliding lid with a gasket sealed impeller shaft. Naturally the device need not be cylindrical and a spherical configuration with a spherical impeller – the levitated scenario – may be attractive. But pursuing this idea would require a different 'dye injection' mechanism. The ideal system may be one where lasers focused on a small volume produce an *in situ* dye with a finite lifetime, thus producing an internally generated dye stream.

Appendix. Additional experimental notes

Water significantly reduces the viscosity of glycerine (a 1% water addition to pure glycerine results in about a 20% decrease in viscosity at room temperature). The viscosity of the working fluid should be checked frequently.

A useful guide to dye selection is a publication by Eastman Kodak entitled 'Kodak Laser Dyes' (Publication JJ-169). Unfortunately this is no longer in print.

Several comments should be made regarding the use of NaI to alter the refractive index. Figure 23 shows the effect of NaI on the refractive index of glycerine. Caution should be exercised while using NaI as it will accelerate corrosion of all unprotected surfaces. Steel clamps, screws, and wires are all subject to rapid rusting over the course of a few weeks. Beware of this, especially for sensitive equipment or machined surfaces. Since glycerine tends to coat and stick rather well, special attention should be taken when cleaning up spills and drips. Also, the iodine will also leave yellow stains that only become apparent after a prolonged period.

REFERENCES

ACHARYA, N., SEN, M. & CHANG H. C. 1992 Heat-transfer enhancement in coiled tubes by chaotic mixing. *Intl J. Mass Heat Transfer* **35**, 2475–2489.

AREF, H. 1984 Stirring by chaotic advection. *J. Fluid Mech.* **143**, 1–21.

ARIS, R. 1962 *Vectors, Tensors, and The Basic Equations of Fluid Mechanics*. Prentice-Hall.

ARNOLD, V. I. 1963 Small denominators and problems of stability of motion in classical and celestial mechanics. *Russian Math. Surveys* **18**, 85–191.

ARNOLD, V. I. 1966 Sur la geometrie differentielle des groupes de Lie de dimension infinie et ses applications I. L'hydrodynamique des fluides parfaits. *Ann. Inst Fourier* **16**, 316–361.

ARNOLD, V. I. 1978 *Mathematical Methods of Classical Mechanics*. Springer.

ASHWIN, P. & KING, G. P. 1995 Streamline topology in eccentric Taylor vortex flow. *J. Fluid Mech.* **285**, 215–247.

ASHWIN, P. & KING, G. P. 1997 A study of particle paths in non-axisymmetric Taylor-Couette flows. *J. Fluid Mech.* **338**, 341–362.

BALASURIYA, S., JONES, C.K.R.T. & SANDSTEDE, B. 1998 Viscous perturbations of vorticity-conserving flows and separatrix splitting. *Nonlinearity* **11**, 47–77.

BAJER, K. & MOFFATT, H. K. 1990 On a class of steady confined Stokes flows with chaotic streamlines. *J. Fluid Mech.* **212**, 337–363.

BAJER, K. & MOFFATT, H. K. 1992 Chaos associated with fluid inertia. In *Topological Aspects of the Dynamics of Fluids and Plasmas* (ed. H. K. Moffatt, G. M. Zaslavsky, M. Tabor & P. Comte). Kluwer.

BATCHELOR, G. K. 1967 *An Introduction to Fluid Dynamics*. Cambridge University Press.

BRYDEN, M. D. & BRENNER, H. 1999 Mass-transfer enhancement via chaotic laminar flow within a droplet. *J. Fluid Mech.* **379**, 319–331.

BROWN, M. G. & SMITH, K. B. 1991 Ocean stirring and chaotic low-order dynamics. *Phys. Fluids* **3**, 1186–1192.

CHAIKEN, J., CHEVRAY, R., TABOR, M. & TAN, Q. M. 1986 Experimental study of Lagrangian turbulence in Stokes flow. *Proc. R. Soc. Lond.* A **408**, 165–174.

CHENG, C.-Q. & SUN, Y.-S. 1990 Existence of invariant tori in three-dimensional measure-preserving mappings. *Celestial Mech.* **47**, 275–292.

CHIEN, W.-L. RISING, H. & OTTINO, J. M. 1986 Laminar mixing and chaotic mixing in several cavity flows. *J. Fluid Mech.* **170**, 355–377.

DANESCU, R. I. & ZUMBRUNNEN, D. A. 1998 Creation of conducting networks among particles in polymer melts by chaotic mixing. *J. Thermoplastic Composite Mater.* **11**, 299–320.

DOMBRE, T., FRISCH, U., GREEN, J. M., HÉNON, M., MEHR, A. & SOWARD, A. M. 1986 Chaotic streamlines in the ABC flows. *J. Fluid Mech.* **167**, 353–391.

FEINGOLD, M., KADANOFF, L. P. & PIRO, O. 1988 Passive scalars, 3-dimensional volume-preserving maps. *J. Statist. Phys.* **50**, 529–565.

FRANJIONE, J. G. & OTTINO, J. M. 1991 Stretching in duct flows. *Phys. Fluids.* A **3**, 2819–2821; erratum 1994 *Phys. Fluids* **6**, 3501.

HALLER, G. & MEZIĆ, I. 1998 Reduction of three-dimensional, volume-preserving flows by symmetry. *Nonlinearity* **11**, 319–339.

HARVEY, A. D. & ROGERS, S. E. 1996 Steady and unsteady computation of impeller-stirred reactors. *AIChE J.* **42**, 2701–2712.

HELLEMAN, R. G. H. 1980 Self generated chaotic behavior in nonlinear mechanics. In *Fundamental problems in statistical mechanics V* (ed. E. G. D. Cohen), pp. 165–275. North Holland.

HÉNON, M. 1966 Sur la topologie des lignes de courant dans un cas particulier. *C.R. Acad. Sci. Paris* A **262**, 312–314.

HOLM, D. D. & KIMURA, Y. 1991 Zero-helicity Lagrangian kinematics of 3-dimensional advection. *Physics Fluids* A **3**, 1033–1038.

HOLMES, P. 1984 Some remarks on chaotic particle paths in time-periodic, three-dimensional swirling flows. *Contemp. Maths.* **28**, 393–404.

JOSEPH, B. & SWATHI, P. S. 1999 Lagrangian particle transport in the Indian Ocean: A model study. *J. Geophys. Res.* **104**, 5211–5224.

KELLOGG, L. H. & STEWART, C. A. 1991 Mixing by chaotic advection in an infinite Prandtl number fluid and implications for mantle convection. *Phys. Fluids* A **3**, 1374–1378.

KHAKHAR, D. V., FRANJIONE, J. G. & OTTINO, J. M. 1987 A case study of chaotic mixing in deterministic flows: the partitioned pipe mixer. *Chem. Engng Sci.* **42**, 2909–2926.

KHAKHAR, D. V., RISING, H. & OTTINO, J. M. 1986 An analysis of chaotic mixing in two model flows. *J. Fluid Mech.* **172**, 419–451.

KROUJILINE, D. & STONE, H. A. 1999 Chaotic streamlines in steady bounded three-dimensional Stokes flows. *Physica* D **130**, 105–132.

KUSCH, H. A. & OTTINO, J. M. 1992 Experiments on mixing in continuous flows. *J. Fluid Mech.* **236**, 319–348.

LAMBERTO, D. J., ALVAREZ, M. M. & MUZZIO, F. J. 1999 Experimental and computational investigation of the laminar flow structure in a stirred tank. *Chem. Engng Sci.* **54**, 919–941.

LAMBERTO, D. J., MUZZIO, F. J., SWANSON, P. D. & TONKOVICH, A. L. 1996 Using time-dependent RPM to enhance mixing in stirred vessels. *Chem. Engng Sci.* **51**, 733–741.

LICHTENBERG, A. J. & LIEBERMAN, M. A. 1992 *Regular and Chaotic Dynamics*. Springer.

MACKAY, R. S. 1994 Transport in 3-D volume-preserving flows. *J. Nonlinear Sci.* **4**, 329–354.

MEZIĆ, I. 1994 On geometrical and statistical properties of dynamical systems: theory and applications. PhD Thesis, California Institute of Technology.

MEZIĆ, I. 1998 Three-dimensional chaotic advection in bounded Navier-Stokes flows. Submitted to *J. Fluid Mech.*

MEZIĆ, I. 1999 Dynamics and transport in volume-preserving maps and flows. Submitted to *Physica* D.

MEZIĆ, I. & WIGGINS, S. 1994 On the integrability and perturbation of three dimensional fluid flows with symmetry. *J. Nonlinear Sci.* **4**, 157–194.

MOSER, J. 1968 On the theory of quasiperiodic motions. *SIAM Rev.* **8**, 145–172.

NAGATA, S. 1975 *Mixing: Principles and Applications*. Halsted Press, New York.

NAGATA, S., YANAGIMOTO, M. & YOKOYAMA, T. 1957 A Study on the mixing of high-viscosity liquid. *Kagaku Kogaku* **21**, 278–286.

OTTINO, J. M. 1989 *The Kinematics of Mixing: Stretching, Chaos and Transport*. Cambridge University Press.

OTTINO, J. M. 1990 Mixing, chaotic advection, and turbulence. *Ann. Rev. Fluid Mech.* **22**, 207–254.

OTTINO, J. M. 1994 Mixing and chemical reactions: a tutorial. *Chem. Engng Sci.* **49**, 4005–4027.

OTTINO, J. M., LEONG, C. W., RISING. H. & SWANSON, P. D. 1988 Morphological structures produced by mixing in chaotic flows. *Nature* **333**, 419–425.

OTTINO, J. M., JANA, S. C. & CHAKRAVARTHY, V. J. 1994 From Reynolds's stretching and folding to mixing studies using horseshoe maps. *Phys. Fluids* A **6**, 685–699.

OTTINO, J. M., MUZZIO, F. J., TJAHJADI, M., FRANJIONE, J. G., JANA, S. C. & KUSCH, H. A. 1992 Chaos, Symmetry, and self-similarity: exploiting order and disorder in mixing processes. *Science* **257**, 754–760.

PEERHOSSAINI, H., CASTELAIN, C. & LEGUER, Y. 1993 Heat-exchanger design based on chaotic advection. *Expl Thermal Fluid Sci.* **7**, 333–344.

PIRO, O. & FEINGOLD, M. 1988 Diffusion in three-dimensional Liouvillian maps. *Phys. Rev. Lett.* **61**, 1799–1802.

REYNOLDS, O. 1894 Study of fluid motion by means of coloured bands. *Nature* **50**, 161–164. This is a transcript of a Friday 2, 1893 evening presentation given by Professor Osborne Reynolds at the Royal Institution (also published in the *Notices of the Proceedings at the Meeting of the Members of the Royal Institution of Great Britain*, Vol. XIV, 1893–1895, pp. 129–138).

REYNOLDS, O. 1901 *Papers on Mechanical and Physical Subjects.* C.J. Clay and Sons, London.

ROM-KEDAR, V. 1988 Part I: An analytical study of transport, mixing and chaos in an unsteady Vortical flow. Part II: Transport in two-dimensional maps. PhD Thesis, California Institute of Technology.

ROM-KEDAR, V. 1990 Transport rates of a family of two-dimensional maps and flows. *Physica* D **43**, 229–268.

ROM-KEDAR, V., LEONARD, A. & WIGGINS, S. 1990 An analytical study of transport, mixing and chaos in an unsteady vortical flow. *J. Fluid Mech.* **214**, 347–394.

ROM-KEDAR, V. & WIGGINS, S. 1990 Transport in two-dimensional maps. *Arch. Rat. Mech. Anal.* **109**, 239–298.

ROM-KEDAR, V. & WIGGINS, S. 1991 Transport in two-dimensional maps: Concepts, examples and a comparison of the theory of Rom-Kedar and Wiggins with the Markov model of MacKay, Meiss and Ott, and Percival. *Physica* D **51**, 248–266.

RUDMAN, M. 1998 Mixing and particle dispersion in the wavy vortex regime of Taylor–Couette flow. *AIChE J.* **44**, 1015–1026.

SOUVALIOTIS, A., JANA, S. C. & OTTINO, J. M. 1995 Potentialities and limitations of mixing simulations. *AIChE J.* **41**, 1605–1621.

STONE, H. A., NADIM, A. & STROGATZ, S. H. 1991 Chaotic streamlines inside drops immersed in steady Stokes flows. *J. Fluid Mech.* **232**, 629–646.

SWANSON, P. D. & OTTINO, J. M. 1990 A comparative computational and experimental study of chaotic mixing of viscous fluids. *J. Fluid Mech.* **213**, 227–249.

TJAHJADI, M. & FOSTER, R. W. 1995 Single screw extruder capable of generating chaotic mixing. USA. Patent 5,551,777.

VILLÉON, J. DE LA, BERTRAND, F., TANGUY, P. A., LABRIE, R., BOUSQUET, J. & LEBOUVIER, D. 1998 Numerical investigation of mixing efficiency of helical ribbons. *AIChE J.* **44**, 972–977.

WIGGINS, S. 1990 *Introduction To Applied Nonlinear Dynamical Systems and Chaos.* Springer.

WIGGINS, S. 1991 *Chaotic Transport in Dynamical Systems.* Springer.

YANNACOPOULOS, T., MEZIĆ, I., KING, G. P. & ROWLANDS, C. 1998 Eulerian diagnostics for Lagrangian chaos in three dimensional Navier-Stokes flows. *Phys. Rev.* E **57**, 482–490.